

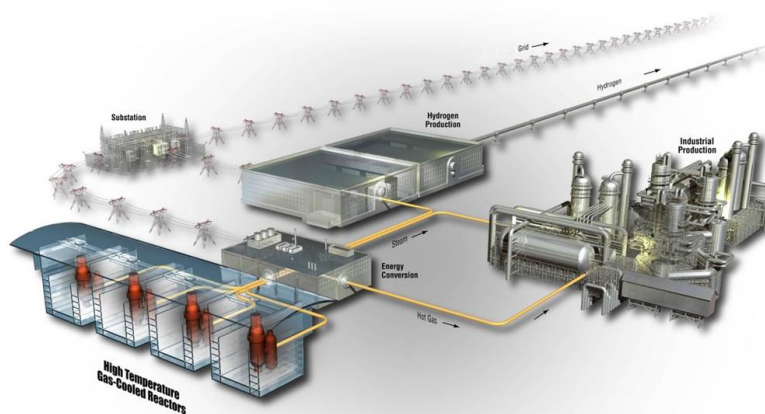


# Tritium Transport Phenomena in Molten-Salt Reactors

June 2021

## *Molten-Salt Tritium Transport Experiment Design*

Thomas F. Fuerst  
Paul W. Humrickhouse  
Chase N. Taylor  
*Idaho National Laboratory*



*INL is a U.S. Department of Energy National Laboratory  
operated by Batelle Energy Alliance, LLC*

#### **DISCLAIMER**

This information was prepared as an account of work sponsored by an agency of the U.S. Government. Neither the U.S. Government nor any agency thereof, nor any of their employees, makes any warranty, expressed or implied, or assumes any legal liability or responsibility for the accuracy, completeness, or usefulness, of any information, apparatus, product, or process disclosed, or represents that its use would not infringe privately owned rights. References herein to any specific commercial product, process, or service by trade name, trade mark, manufacturer, or otherwise, does not necessarily constitute or imply its endorsement, recommendation, or favoring by the U.S. Government or any agency thereof. The views and opinions of authors expressed herein do not necessarily state or reflect those of the U.S. Government or any agency thereof.

# **Tritium Transport Phenomena in Molten-Salt Reactors**

## **Molten-Salt Tritium Transport Experiment Design**

**Thomas F. Fuerst  
Paul W. Humrickhouse  
Chase N. Taylor  
Idaho National Laboratory**

**June 2021**

**Idaho National Laboratory  
Advanced Reactor Technologies  
Idaho Falls, Idaho 83415**

**<http://www.ART.INL.gov>**

**Prepared for the  
U.S. Department of Energy  
Office of Nuclear Energy  
Under DOE Idaho Operations Office  
Contract DE-AC07-05ID14517**

*Page intentionally left blank*



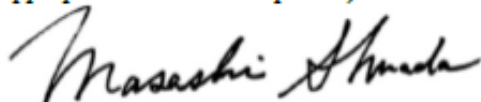
INL ART Program

# Tritium Transport in Molten-Salt Reactors

INL EXT-21-63108

June 2021

Technical Reviewer: (Confirmation of mathematical accuracy, and correctness of data and appropriateness of assumptions.)



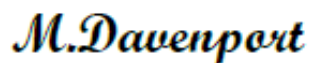
---

Masashi Shimada  
Star Experiments Lead

---

06/17/2021  
Date

Approved by:



---

Michael E. Davenport  
INL ART Project Manager

---

6/24/21

---

Date



---

Travis R. Mitchell  
INL ART Program Manager

---

6/24/2021

---

Date



---

Michelle T. Sharp  
INL Quality Assurance

---

6/24/21

---

Date

## ABSTRACT

Tritium is produced from neutron interactions with both lithium and beryllium. Large quantities of tritium are generated in Molten-Salt Reactors (MSRs) that use  $\text{LiF/BeF}_2$  (FLiBe) as the fuel salt. Tritium is unique among radionuclide hazards since it readily permeates through metal structural materials at high temperatures; all metal surfaces are therefore potential release paths for tritium. For adequate safety analysis and eventual licensing of new reactors, predictive models for tritium transport and release from MSRs must be developed. These models must account for the multiple transport phenomena involved with tritium: fuel salt-phase mass transport, dissociation/recombination reactions on metal surfaces, interstitial diffusion through the metal structure, and salt- or gas-phase mass transport in the downstream fluid. These models also must also be validated with representative experiments.

Our previous report outlined tritium transport phenomena involved in MSRs, made suggestions on gaps in the transport data set, and proposed an experimental test stand to test combined transport effects—tritium transport through pipe walls in a convective salt flow.

In this report, we summarize an updated analysis framework for tritium transport in MSRs, report our results on hydrogen and deuterium permeation through Hastelloy N, and describe the final design of the Molten-Salt Tritium Transport Experiment (MSTTE, pronounced “misty”). The Molten-Salt Reactor Experiment (MSRE) provides the only wholistic experimental data set for tritium transport in MSRs and understanding the transport phenomena involved in the MSRE is crucial for future model development. One set of parameters in our analysis framework was unknown for the MSRE—surface reaction rates for tritium on Hastelloy N. This warranted our hydrogen and deuterium permeation campaign to assess the permeability, diffusivity, and solubility of hydrogen isotopes in clean Hastelloy N. Surface reaction rate constants were probed by low-pressure measurements; however, no surface effects were observed in the limits of our permeation apparatus. Permeation experiments on oxidized Hastelloy N were not performed for this report but are planned in future work. The experimental test stand, MSTTE, measures combined transport properties of the salt-metal system. MSTTE is a forced convection FLiBe loop with custom designed test section to measure tritium transport through candidate structural materials. We use MSRE relevant dimensionless numbers to design and scale the test section. Hastelloy N is a candidate loop and test section material due to the relevance for the MSRE and related designs; however, other metals are being considered (e.g., 316H SS) which may better align with current vendor concepts.

## **ACKNOWLEDGEMENTS**

This work of authorship was prepared as an account of work sponsored by Idaho National Laboratory (under Contract DE-AC07-05ID14517), an agency of the U.S. Government. Neither the U.S. Government, nor any agency thereof, nor any of their employees makes any warranty, express or implied, or assumes any legal liability or responsibility for the accuracy, completeness, or usefulness of any information, apparatus, product, or process disclosed, or represents that its use would not infringe privately owned rights.

*Page intentionally left blank*

# CONTENTS

ABSTRACT.....	iv
ACKNOWLEDGEMENTS.....	v
ACRONYMS.....	xi
1. Introduction.....	1
2. MSR Tritium Transport Analysis.....	1
2.1 Tritium Transport Phenomena .....	1
2.2 MSRE Mass Transport.....	3
2.3 MSRE Tritium Transport Analysis .....	5
3. Hastelloy N Permeation Campaign.....	9
3.1 Sample Information, Preparation, and Characterization .....	9
3.2 Permeation Apparatus .....	12
3.3 Permeation Theory and Analysis .....	14
3.4 Permeation Results.....	15
4. The Molten-Salt Tritium Transport Experiment .....	20
4.1 Experiment Overview .....	20
4.2 Major Equipment/Components .....	23
4.2.1 Test Section.....	23
4.2.2 Permeate Gas Analysis System.....	24
4.2.3 Plenum .....	24
4.2.4 Reverse Permeator Unit .....	25
4.2.5 Molten-Salt Pump .....	25
4.2.6 Flow Meter and Pressure Gauge .....	26
4.2.7 Supply Tank .....	26
4.2.8 Differential Gas Sensor.....	27
4.3 Safety Considerations .....	29
4.4 Experiment Analysis .....	30
4.4.1 Test Section Scaling.....	30
5. Summary .....	34
6. References.....	34

## FIGURES

Figure 1. The permeation number (W) for tritium transport in salt-metal components of MSRE. ....	7
Figure 2. The transport number (H) for tritium transport in salt-metal components of MSRE. H $\ll 1$ indicates surface reactions are rate-limiting relative to mass transport in the salt; H $\gg 1$ indicates mass transport is rate-limiting relative to surface reactions. ....	8
Figure 3. W/H for tritium transport in the salt-metal components of MSRE.....	9
Figure 4. Photo of as-received Hastelloy N sheet and nominal composition from Haynes International, Inc.....	10
Figure 5. SEM image of as-prepared Hastelloy N surface taken at 10 kV and 2 kX.....	10
Figure 6. EBSD image of as-prepared Hastelloy N sample (a) pre-permeation testing and (b) post- permeation testing.....	11
Figure 7. AES survey scans pre- and post-DP with 3 kV electrons. Major elements are labelled at the top. ....	11
Figure 8. AES depth profile of Hastelloy N.....	12
Figure 9. SEM images taken post sputtering at 3kV.....	12
Figure 10. Photo of the SGAP apparatus at INL.....	13
Figure 11. Sample sealing and housing in SGAP. ....	13
Figure 12. D <sub>2</sub> flux vs. pressure from the buildup method. ....	16
Figure 13. Diffusivity from the rise method calculated from characteristic time (left) and NLSR fitting (right). ....	16
Figure 14. Diffusivity from the evolution method calculated from characteristic time (left) and NLSR fitting (right). ....	17
Figure 15. Arrhenius plot of hydrogen isotope permeability in Hastelloy N and literature comparisons [20-22]. ....	17
Figure 16. Arrhenius plot of hydrogen isotope diffusivity in Hastelloy N. ....	18
Figure 17. Arrhenius plot of hydrogen isotope solubility in Hastelloy N.....	19
Figure 18. Dissociation rate constant $kd$ , for select metals included in Table 3 as well as the lower bound values for Hastelloy N from this study. ....	19
Figure 19. Piping and instrumentation diagram of the test loop (MSTTE). Grey indicates the gas distribution system (1/4" VCR fittings), blue indicates the permeate gas analysis system (also 1/4" VCR and CF-flange components), red indicates the molten-salt loop (1" Swagelok fittings), and green indicates the redox/plenum gas system (1/4" VCR and CF-flange components). ....	21
Figure 20. Example of similar test section used in the PreTEX experiment at INL. ....	24
Figure 21. Reverse permeator design.....	25
Figure 23. Schematic of the differential gas sensor. ....	29
Figure 24. Calculation of FLiBe flow rate (lpm) as a function of test section ID (mm) to meet MSRE relevant Re number. ....	30

Figure 25. Total loop head loss calculations as a function of test section ID for (A) 0.5-inch OD loop structural tubing and (B) 1-inch OD loop structural tubing.....	31
Figure 26. H number vs. FLiBe flow rate (lpm) for Cases 1–3. Calculated for IDs of 2, 5, 8, 10, 15, and 20 mm at a temperature of 650°C.....	32
Figure 27. W number vs. hydrogen partial pressure (Pa) for Case 1, Case 3, and Case 5. Calculated for wall thicknesses of 0.2, 0.3, 0.5, 1, 1.5, and 2 mm at a temperature of 650°C.....	33

## TABLES

Table 1. Select properties of FLiBe from [5] and tritium diffusivity from [6]. .....	4
Table 2. Design specifications and dimensionless numbers for each component of the salt-metal interaction system taken from [3]. .....	4
Table 3. Hydrogen dissociation rate constant ( $k_d$ ) of Ni and high-Ni superalloys.....	5
Table 4. Summary of Henry’s law constants of hydrogen isotopes in FLiBe. ....	6
Table 5. Major equipment table including symbols, manufacturer, and product number for MSTTE. ....	21

*Page intentionally left blank*



## ACRONYMS

AES	Auger electron spectroscopy
ASME	American Society of Mechanical Engineers
CF	ConFlat
CSI	Centering ring, Sealing element, Inner ring
DP	Depth profiling
EBSD	Electron backscatter diffraction
FHR	Fluoride salt-cooled high-temperature reactor
FLiBe	LiF/BeF <sub>2</sub>
HEPA	High-efficiency particulate air
ID	Inner diameter
INL	Idaho National Laboratory
MGLC	Membrane Gas-Liquid Contactor
MSR	Molten-Salt Reactor
MSRE	Molten-Salt Reactor Experiment
MSTTE	Molten-Salt Tritium Transport Experiment
NLSR	Nonlinear least squares regression
OD	Outer diameter
ORNL	Oak Ridge National Laboratory
P&ID	Piping and instrumentation diagram
QMS	Quadrupole mass spectrometer
RGA	Residual gas analyzer
SAM	Scanning Auger Microprobe
SEM	Scanning Electron Microscope
SGAP	Static Gas Absorption Permeation
SS	Stainless Steel
STAR	Safety and Tritium Applied Research Facility
TEX	Tritium Extraction eXperiment
TGAP	Tritium Gas Absorption Permeation
UHP	Ultra high purity
UHV	Ultra high vacuum
VCR	Vacuum coupling radiation

*Page intentionally left blank*

# Tritium Transport in Molten-Salt Reactors

## 1. Introduction

Molten-salt reactors (MSRs) that make use of lithium and/or beryllium salts in the fuel (or core coolant in the case of fluoride salt-cooled high-temperature reactors [FHRs]), such as FLiBe, will generate significant quantities of tritium relative to other fission reactor types. While liquid-fueled MSRs will employ an off-gas system for the purpose of removing the many volatile fission products produced during operation, tritium is unique among these since it can diffuse directly through metal structures at the high operating temperatures of a MSR. It therefore constitutes a radiological hazard, and source term, that will be released even during normal steady-state operation without appropriate mitigations. The diffusion, or permeation, process may occur between the point of tritium generation via neutron interactions with Li and Be in the core and potential removal in a sparger to the off-gas system or downstream of the off-gas system for any tritium not successfully removed by it.

Optimal design of the sparging and off-gas system to maximize tritium removal, in combination with other design mitigations that block, capture, or remove tritium from the system, requires first understanding the physical phenomena that govern tritium release from flowing salt systems via permeation. Historically and recently, these have been assumed to consist of (turbulent) diffusion or “mass transport” in the salt, followed by diffusion (or permeation) through the metal wall. In our prior work [1], we identified a third potentially important phenomenon, the reactions at the interface that are necessary to transform molecules dissolved in the fluid to atoms dissolved in the metal, and identified evidence from the Molten-Salt Reactor Experiment (MSRE) that pointed to this (without understanding the underlying mechanism) as a potentially rate-limiting effect in tritium permeation. We incorporated this into a model for tritium transport that includes all three phenomena, which predicts how permeation will scale with geometric and flow parameters and material properties under arbitrary conditions [1], and identifies dimensionless numbers that determine which (if any) phenomenon is rate-limiting. This is summarized in Section 2.1.

The surface reactions introduce additional physical constants that are not known for MSRE materials (i.e. Hastelloy N), and so we performed low-partial pressure permeation measurements in Hastelloy N in an attempt to measure these. These experiments are described in Section 3. The next step is to perform a scaled experiment that integrates these effects in MSR-relevant materials and conditions (i.e., in a flowing high-temperature salt in contact with a solid metal membrane through which tritium will permeate). Such an experiment will provide validation data for the comprehensive model or lead to the development of alternate models if appropriate. This report’s primary topic is the scaling analysis and design of this experiment.

## 2. MSR Tritium Transport Analysis

### 2.1 Tritium Transport Phenomena

Tritium transport phenomena were discussed in detail in our previous report [1]. Here we provide a brief overview to introduce the symbols and terminology.

Tritium transport begins with generation in the fuel salt. Transport out of the salt and to all other systems first involves transport within the salt itself to a system interface. This process is referred to as “mass transport” and is described by the equation:

$$Q = k_T A (C_L - C_i) \quad (1)$$

where  $Q$  is the flow rate of tritium ( $\text{mol T}_2 \text{ s}^{-1}$ ),  $A$  is the surface area ( $\text{m}^2$ ),  $k_T$  is the mass transport coefficient ( $\text{m s}^{-1}$ ),  $C_L$  is the concentration of  $\text{T}_2$  in the bulk salt ( $\text{mol T}_2 \text{ m}^{-3}$ ), and  $C_i$  is the concentration of  $\text{T}_2$  at the surface of the interface of the salt and metal ( $\text{mol T}_2 \text{ m}^{-3}$ ).

At the interface of the solid metal structural material, molecular tritium must be dissociated into atomic form to diffuse through the metal lattice. The net flow across the interface is defined by the difference between the dissociation and recombination rates:

$$Q = k_d A P_i - k_r A C_s^2 \quad (2)$$

where  $k_d$  is the dissociation rate constant ( $\text{mol T}_2 \text{ m}^{-2} \text{ s}^{-1} \text{ Pa}^{-1}$ ),  $k_r$  is the recombination rate constant ( $\text{m}^4 \text{ mol T}_2^{-1} \text{ s}^{-1}$ ),  $P_i$  is the tritium partial pressure at the interface (Pa), and  $C_s$  is the tritium concentration in the solid at the surface ( $\text{mol T}_2 \text{ m}^{-3}$ ). The tritium partial pressure and concentration in salt ( $C$ ) are assumed to be related by Henry's law:

$$C = K_H P \quad (3)$$

Where  $K_H$  is the Henry's law constant ( $\text{mol T}_2 \text{ m}^{-3} \text{ Pa}^{-1}$ ), which is used when tritium is dissolved molecularly ( $\text{T}_2$ ) into a fluid (e.g., the molten-salt system).

In equilibrium between molecular tritium in the gas (or salt) phase and the atomic tritium dissolved in the metal phase, the recombination rate is equal to dissociation rate, and we arrive at Sieverts' law:

$$C = \sqrt{\left(\frac{k_d}{k_r} P\right)} = K_S \sqrt{P} \quad (4)$$

Where  $K_S$  is Sieverts' constant, also known as solubility ( $\text{mol T}_2 \text{ m}^{-3} \text{ Pa}^{-0.5}$ ), which is used when tritium is dissolved in atomic form (T) into metals.

Once tritium is dissolved into the metal it is transported via the concentration gradient obeying Fick's 2<sup>nd</sup> law:

$$Q = -A D_T \frac{\partial C}{\partial x} \quad (5)$$

Where  $D_T$  is the diffusion coefficient of tritium through the metal lattice ( $\text{m}^2 \text{ s}^{-1}$ ).

On the downstream side surface, the reverse process of Equation (2) occurs where tritium recombines to molecular form and desorbs from the surface and is transported into the downstream fluid system via the reverse of Equation (1). All analyses herein make the simplifying assumption that both sides of the structure are "symmetric," i.e. that their dissociation and recombination rates are identical.

When interstitial diffusion through the metal lattice is rate-limiting, the surface reactions are assumed in quasi-equilibrium and Equation (5) becomes Richardson's equation:

$$Q = \frac{A \Phi}{l} \left[ \sqrt{P_{T_2,1}} - \sqrt{P_{T_2,2}} \right] \quad (6)$$

Where  $l$  is the thickness of the metal (m),  $\Phi = D_T K_S$  is the permeability of tritium in the metal ( $\text{mol T}_2 \text{ m}^{-1} \text{ s}^{-1} \text{ Pa}^{-0.5}$ ), and the subscripts (1 and 2) indicate the upstream and downstream side, respectively.

While the net flux through a pipe wall is generally a complicated function of all three transport phenomena, one can identify limiting cases in which only one is rate-limiting. Since there are three transport processes, two dimensionless numbers characterize these limiting regimes. The first, the permeation number ( $W$ ) [2], is the ratio of diffusion resistance to surface resistance. When  $W \gg 1$ ,

diffusive transport resistance is much larger than surface reaction resistance and, therefore, is rate-limiting relative to it. When  $W \ll 1$ , surface reaction resistance dominates diffusion resistance.

$$W = \frac{k_d t P^{0.5}}{\Phi} = \frac{k_d t}{\Phi} \sqrt{\frac{C}{K_H}} \quad (7)$$

The second, what we will call the transport number (H), describes the ratio of mass transport resistance to surface resistance. When  $H \gg 1$ , mass transport resistance dominates surface resistance and is therefore rate-limiting relative to it. When  $H \ll 1$ , surface reaction resistance dominates mass transport resistance.

$$H = \frac{k_d}{k_T K_H} \quad (8)$$

One can therefore identify the three limiting regimes based on the values of W and H. Permeation is :

- Mass transport limited when  $H \gg 1$  and  $H/W \gg 1$ ;
- Surface limited when  $W \ll 1$  and  $H \ll 1$ ;
- Diffusion limited when  $W \gg 1$  and  $W/H \gg 1$ .

## 2.2 MSRE Mass Transport

Unlike the other physical constants described in Section 2.1, which are material properties, the mass transport coefficient ( $k_T$ ), which characterizes the transport of tritium between the salt and the metal surface, must be obtained by an analysis or correlation. In the original tritium distribution analysis of MSRE [3], these coefficients were calculated with the Dittus-Boelter correlation, using the analogy between mass and heat transfer. This relation is shown in Equation (9), where the Sherwood number (Sh) is the mass transfer analogue of the Nusselt number (Nu) in heat transfer, which depends on the Reynolds number (Re) and Schmidt number (Sc):

$$Sh = 0.023 (Re^{0.8})(Sc^{0.4}) \quad (9)$$

Sh is defined by Equation (10) as the ratio between convective mass transport and diffusive mass transport.  $k_T$  is the mass transport coefficient ( $m s^{-1}$ ), L is the characteristic length (m, see discussion below), and  $D_T$  is tritium diffusion in the salt ( $m^2 s^{-1}$ ).

$$Sh = \frac{k_T L}{D_T} \quad (10)$$

The Reynolds number (Re), shown in Equation (11), is the ratio of inertial forces to viscous forces of a fluid.  $\rho$  is the density of the fluid ( $kg m^{-3}$ ),  $v$  is the fluid velocity ( $m s^{-1}$ ), and  $\mu$  is the dynamic viscosity of the fluid (Pa s).

$$Re = \frac{\rho v L}{\mu} \quad (11)$$

The Schmidt number (Sc), shown in Equation (12), is the ratio of kinematic viscosity to diffusivity.

$$Sc = \frac{\mu}{\rho D_T} \quad (12)$$

Using these dimensionless numbers allows us to scale the conditions of the various salt-metal components in MSRE to the lab-scale experiment. Table 1 lists the density, dynamic viscosity, and diffusivity used to calculate the Schmidt number. The mass transport coefficients reported in [3] and the properties in Table 1 are used to calculate the Sherwood number. Finally, the Reynolds number is obtained from solving Equation (9) with the Sherwood and Schmidt numbers.

Table 2 displays the calculated dimensionless numbers as well as other select information of the salt-metal components such as wall thickness, surface area, average temperature, salt flow rate, and mass transport coefficients.

The characteristic length used in the dimensionless numbers is the relevant length scale for each component. For flow through circular ducts, the characteristic length is the hydraulic diameter defined by the inner diameter of the piping. This definition is used for the following systems: primary system tubes, secondary system piping, heat exchanger tubes, and radiator tubes. The characteristic length of the heat exchanger shell-side is described by [4]:

$$L_{shell} = \frac{4 \left( \frac{\sqrt{3} P_t^2}{4} - \frac{\pi d_o^2}{8} \right)}{\pi d_o / 2} \quad (13)$$

Table 1. Select properties of FLiBe from [5] and tritium diffusivity from [6].

Salt	Melting Point	Boiling Point	Density	Dynamic Viscosity	Diffusivity
	[K]	[K]	[kg m <sup>-3</sup> ]	[Pa s]	[m <sup>2</sup> s <sup>-1</sup> ]
FLiBe	732	1703	2413 – 0.488 · T[K]	$1.16 \times 10^{-4} \exp\left(\frac{3755}{T[K]}\right)$	$9.3 \times 10^{-7} \exp\left(\frac{-42 [K] \text{ mol}^{-1}}{RT[K]}\right)$
Evaluated at T = 565°C			$2.0 \times 10^3$	$1.0 \times 10^{-2}$	$2.2 \times 10^{-9}$
Evaluated at T = 650°C			$2.0 \times 10^3$	$6.8 \times 10^{-3}$	$3.9 \times 10^{-9}$

Table 2. Design specifications and dimensionless numbers for each component of the salt-metal interaction system taken from [3].

Component (Salt)	Surface Area A <sub>T</sub> (cm <sup>2</sup> )	Charact. Length L (cm)	Wall Thickness t (mm)	Flow Rate f (cm <sup>3</sup> s <sup>-1</sup> )	Avg. T T <sub>a</sub> (°C)	Mass Transport k <sub>T</sub> (cm s <sup>-1</sup> )	Sherwood Number Sh	Schmidt Number Sc	Reynolds Number Re
Wall of Reactor Vessel (Fuel)	1.0E5	5.1	15	4700	650	6E-3	7.8E2	8.8E2	1.6E4
Primary System Piping (Fuel)	4.6E4	12.8	6.6	4700	650	13E-3	4.3E3	8.8E2	1.3E5
Heat Exchanger Shell (Fuel)	3.2E4	2.10	13	4700	650	6E-3	3.2E2	8.8E2	5.1E3

Heat Exchanger Tubes (Fuel)	2.4E5 (159 tubes)	1.1	1.1	4700	650	8E-3	2.2E2	8.8E2	3.2E3
Heat Exchanger Tubes (Coolant)	2.4E5 (159 tubes)	1.1	1.1	950	565	13E-3	3.9E2	2.3E3	4.0E3
Secondary System Piping (coolant)	2.3E5	12.8	6.6	950	565	7E-3	4.0E3	2.3E3	7.4E4
Radiator Tubes (coolant)	6.5E5 (120 tubes)	1.5	1.8	950	565	7E-3	4.8E2	2.3E3	5.3E3

## 2.3 MSRE Tritium Transport Analysis

In the MSRE tritium distribution calculations [3, 7, 8] (and subsequent codes and analyses for FHRs and MSR [9-12]), tritium transport through the structural materials was modeled considering only mass transport through the salt Equation (1) and diffusion-limited permeability through the metals Equation (6). The best agreement with measured tritium distributions in the MSRE was achieved only with the following model adjustments:

- Mass transport coefficients were reduced by a factor of 2
- Permeability of the metal was reduced by a factor of 1,000 from reference values.

Overall permeation in the MSRE was generally though limited by mass transport, but even these coefficients had to be reduced in order to achieve good agreement with the data. A variety of possible explanations for this were offered; one was that “oxide on the metal surfaces or a change from Q proportional to  $p^{1/2}$  to Q proportional to  $p^1$  at very low pressures might produce such a reduction in the effective permeability of the metal.” This had been observed in some low-partial pressure experiments with metals by that time but wasn’t yet theoretically understood. It is now well known to arise when the surface kinetic processes described in Equation (2) become rate-limiting, in which case the total permeation flux is proportional to  $k_d$ . In order to ascertain whether this effect was important in the MSRE, it was recommended low-partial pressure permeation measurements be conducted in both clean and oxidized Hastelloy N. It appears this recommendation was never acted on until now, and we describe such measurements made recently at the Idaho National Laboratory (INL) Safety and Tritium Applied Research (STAR) facility in Section 3.4. Similar measurements have been made in the intervening years on other high-nickel superalloys, and the resultant rate constants are summarized in Table 3.

Table 3. Hydrogen dissociation rate constant ( $k_d$ ) of Ni and high-Ni superalloys.

Isotope	Metal	Surface State	Dissociation Coefficient $k_d$ (mol m <sup>-2</sup> s <sup>-1</sup> Pa <sup>-1</sup> )			Reference	Case
			$k_d = k_{d0} \exp\left(-\frac{E_a}{RT}\right)$	650°C	565°C		
H	Pure Ni	Clean	$1.4 \times 10^{-6} \exp\left(-\frac{30}{RT}\right)$	$2.9 \times 10^{-8}$	$1.9 \times 10^{-8}$	[13]	-
D	Inconel 600	Clean	$3.3 \times 10^{-7} \exp\left(-\frac{46}{RT}\right)$	$8.3 \times 10^{-10}$	$4.5 \times 10^{-10}$	[14]	-
T	Inconel 625	Clean	$5.2 \times 10^{-5} \exp\left(-\frac{33}{RT}\right)$	$7.1 \times 10^{-7}$	$4.6 \times 10^{-7}$	[15]	-

T	Inconel 625	Oxidized	$2.6 \times 10^{-1} \exp(-\frac{111}{RT})$	$1.4 \times 10^{-7}$	$3.1 \times 10^{-8}$	[15]	5
H	Incoloy 800	Clean	$4.1 \times 10^{-6} \exp(-\frac{44}{RT})$	$1.3 \times 10^{-8}$	$7.2 \times 10^{-9}$	[16]	-
H	Incoloy 800	Oxidized	$2.7 \times 10^{-10} \exp(-\frac{40}{RT})$	$1.4 \times 10^{-12}$	$8.5 \times 10^{-13}$	[16]	3 & 4
D	Hastelloy N	Clean		$1.4 \times 10^{-6}$	$2.1 \times 10^{-7}$	This work*	1 & 2

\*Note reported values are lower bounds, see Section 3.

A consideration not addressed in the MSRE reports is the more than 1000× span of Henry's law constants of hydrogen species in FLiBe as summarized in our previous report [1]. These data are summarized in Table 4.

Table 4. Summary of Henry's law constants of hydrogen isotopes in FLiBe.

Species	Salt	Henry's Law Constant ( $K_H$ ) [mol m <sup>-3</sup> Pa <sup>-1</sup> ]			Reference	Case
		$K_H = K_{H0} \exp(\frac{E_a}{RT})$	650°C	565°C		
H <sub>2</sub> /D <sub>2</sub>	FLiBe	$2.1 \times 10^{-6} \exp(-\frac{29}{RT})$	$4.8 \times 10^{-8}$	$3.3 \times 10^{-8}$	[17]	2 & 4
T <sub>2</sub>	FLiBe	$7.9 \times 10^{-2} \exp(-\frac{35}{RT})$	$8.3 \times 10^{-4}$	$5.2 \times 10^{-4}$	[6]	1 & 3
T <sub>2</sub>	FLiBe	$\frac{0.06}{T} \exp(-\frac{11(293 - 0.12T)}{T})$	$7.4 \times 10^{-6}$	$5.7 \times 10^{-6}$	[3]	5

In order to understand which transport phenomena were important in the MSRE (and which, if any, were rate-limiting in different components), we have calculated the dimensionless numbers W and H using the parameters defined in

Table 2, Table 3, and Table 4 for a variety of cases, employing different assumptions to account for the range of parameter uncertainties described above. These are:

Case 1: high  $K_H$  and clean metal surfaces

Case 2: low  $K_H$  and clean metal surfaces

Case 3: high  $K_H$  and heavily oxidized metal surfaces

Case 4: low  $K_H$  and heavily oxidized metal surfaces

Case 5: intermediate  $K_H$  and lightly oxidized surface

The high  $K_H$  is taken from Calderoni et al. [6], the low  $K_H$  from Malinauskas et al. [17], and intermediate  $K_H$  from that estimated in the MSRE analysis [3], as noted in Table 4. The clean surface  $k_d$  is taken from the bound values in this study, the heavily oxidized surface  $k_d$  is taken from oxidized Incoloy 800 reported by Esteban et al. [16], and the lightly oxidized  $k_d$  from the data of oxidized Inconel 625 reported by Perujo et al. [15], as noted in Table 3. The permeability of Hastelloy N is taken from the results of this work shown in Section 3.

The permeation number (W) was calculated for each salt-metal system, and the results are shown in Figure 1. Only in Case 2 (clean surfaces and low Henry's law constant) is the diffusion resistance greater than surface resistances across all systems. In Cases 1 and 5, the diffusion resistance is slightly greater than surface resistance in the fuel salt due to the higher average temperature, but the reverse occurs in the coolant salt due to lower average temperature. In Cases 3 and 4 (oxidized surfaces), surface resistance



dominates over diffusion resistance across all systems due to the slow dissociation/recombination rates on oxidized surfaces.

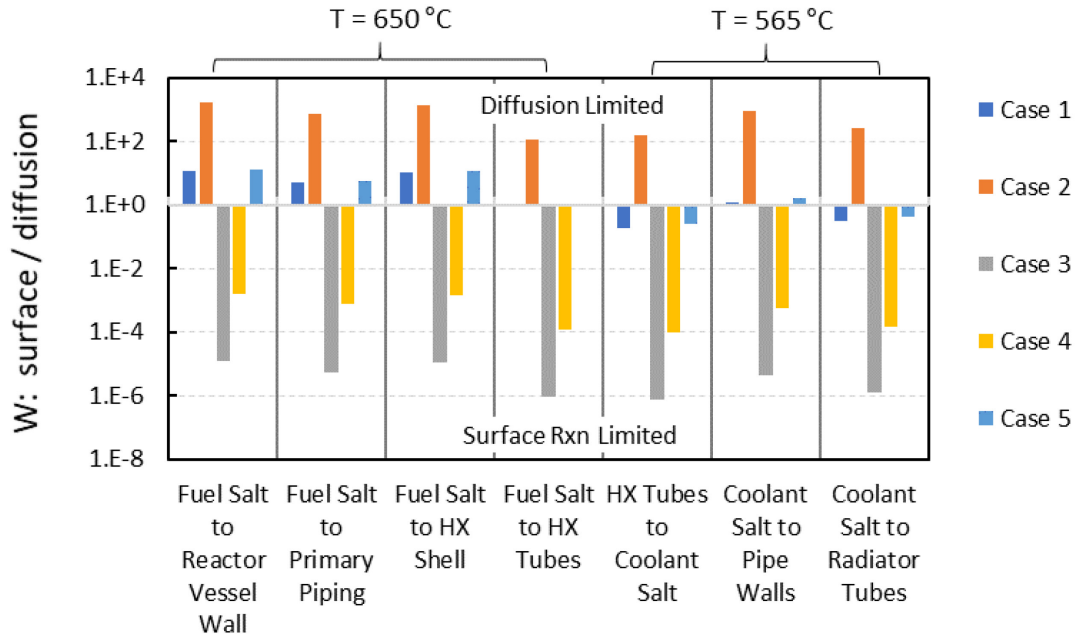


Figure 1. The permeation number (W) for tritium transport in salt-metal components of MSRE.

Figure 2 shows the transport number (H) for each salt-metal system. In the cases with clean or lightly oxidized surfaces (Cases 1, 2, and 5), mass transport resistance in the salt phase is greater than the surface reaction resistance for all the salt-metal systems. In cases with heavily oxidized surfaces (Cases 3 and 4), the surface reaction resistance is greater than mass transport resistance. The upper and lower bound (high and low) Henry's law constant changes the magnitude of the dimensionless number but did not change the transport regime.

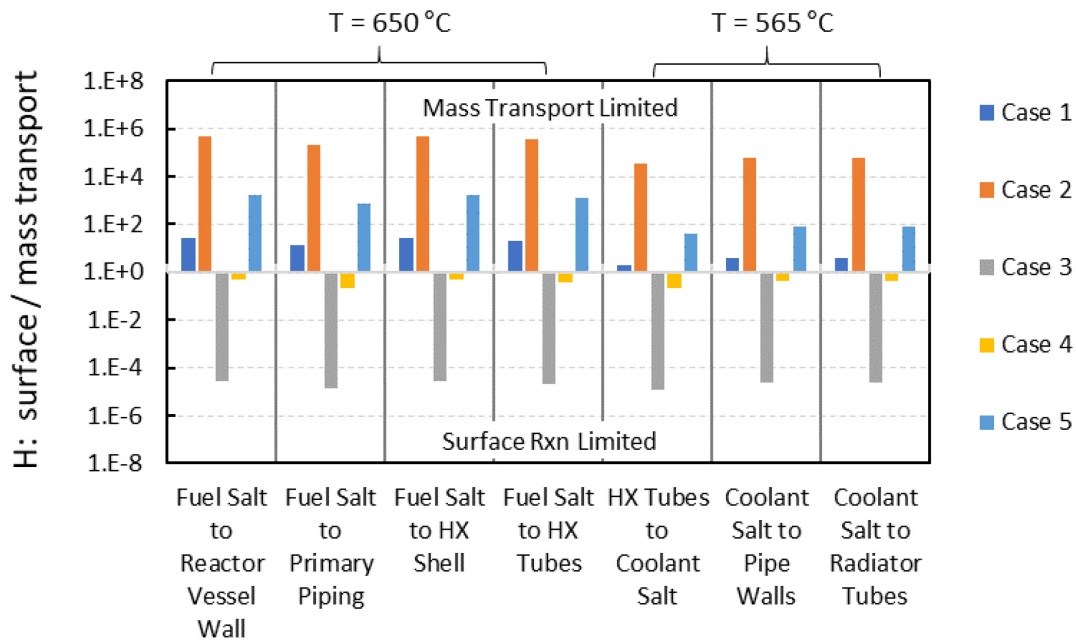


Figure 2. The transport number (H) for tritium transport in salt-metal components of MSRE.  $H \ll 1$  indicates surface reactions are rate-limiting relative to mass transport in the salt;  $H \gg 1$  indicates mass transport is rate-limiting relative to surface reactions.

Finally, the analysis of diffusion resistance relative to mass transport resistance ( $W/H$ ) is assessed for each system as shown in Figure 3. Here, all cases indicate mass transport resistance dominates compared to diffusion resistance, which is consistent with the qualitative conclusions of the original MSRE reports. This allows us to conclude mass transport and surface reactions are the rate-limiting tritium transport processes in the MSRE. Therefore, experimental investigation of these specific transport phenomena is warranted for validating tritium transport models for the safety and licensing of MSRs. This is the primary motivation of the experimental apparatus described in Section 4.

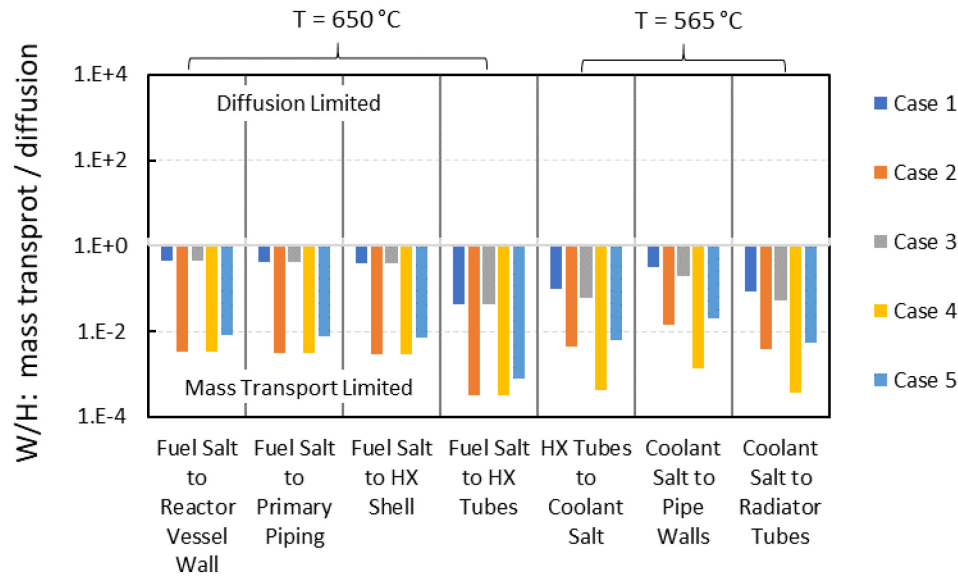


Figure 3. W/H for tritium transport in the salt-metal components of MSRE.

### 3. Hastelloy N Permeation Campaign

To support analysis of MSRE conditions, hydrogen permeation testing of Hastelloy N was conducted to obtain permeability, diffusivity, solubility, and surface reaction rate constants for both hydrogen and deuterium. This section describes the experiments and results for clean Hastelloy N to support this task.

#### 3.1 Sample Information, Preparation, and Characterization

The Hastelloy N samples were prepared from a sheet purchased from Haynes International, Inc. The as-received thickness was  $1.51 \pm 0.01$  mm. Figure 4 shows the nominal composition reported by the manufacturer and a photo of the as-received sheet. Disks with a diameter of 20.6 mm were cut from the sheet. Both sides of the disks were metallographically prepared using a procedure provided by the manufacturer: fine grinding with 320, 400, and 600 grit SiC, rough polishing with a 9  $\mu$ m diamond paste, and vibratory polishing using 0.3  $\mu$ m then 0.05  $\mu$ m  $\text{Al}_2\text{O}_3$ . The samples were washed and cleaned in a sonication bath between each step. The resulting sample thickness post-polishing was  $1.37 \pm 0.01$  mm.

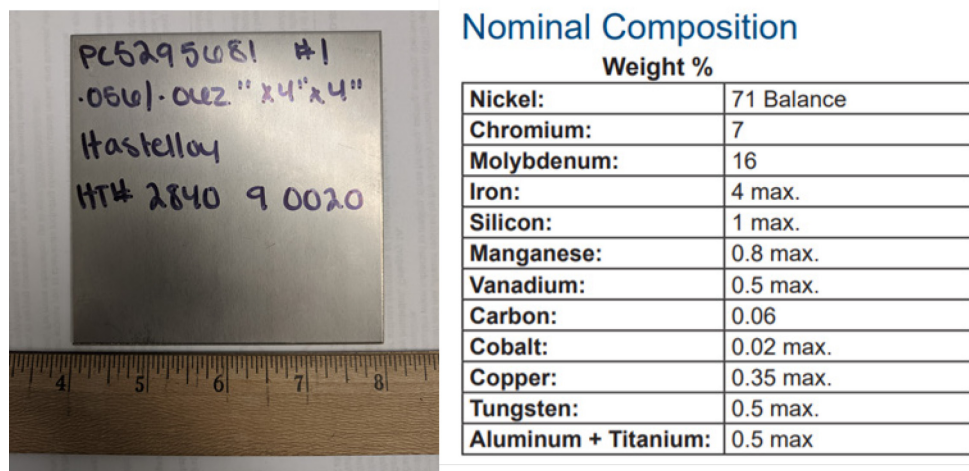


Figure 4. Photo of as-received Hastelloy N sheet and nominal composition from Haynes International, Inc.

A JEOL JSM 6610LV scanning electron microscope (SEM) was used to obtain SEM images and electron backscatter diffraction (EBSD) images of the post-polished, as-prepared Hastelloy N surface as shown in Figure 5 and Figure 6, respectively. The SEM images showed smooth surfaces with major defects such as scratches and large holes removed. Several small pinholes remained on the surface post-polishing. The EBSD images revealed scratches likely produced from the polishing process that remained on the surface. The images also revealed the polycrystalline structure of the Hastelloy N grains. A bimodal grain size distribution including both small 2  $\mu\text{m}$  and large 40  $\mu\text{m}$  grains with an average size of 25.7  $\mu\text{m}$  defined the microstructure pre-permeation testing. The average grain size grew to 47  $\mu\text{m}$  upon permeation testing and heating under UHV for  $\sim 80$  h (500–700°C). The small scratch artifacts from polishing were also removed; however, larger defects were observed (likely caused from sample handling and mounting in the permeation apparatus).

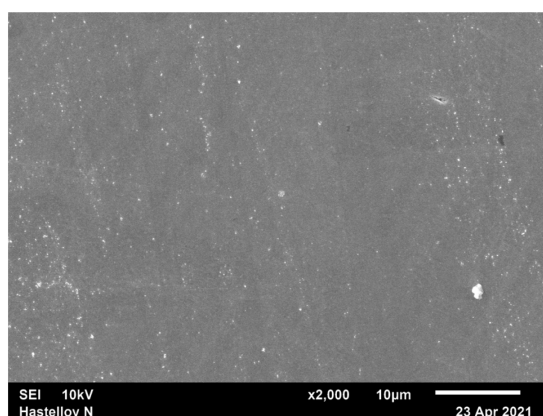


Figure 5. SEM image of as-prepared Hastelloy N surface taken at 10 kV and 2 kX.

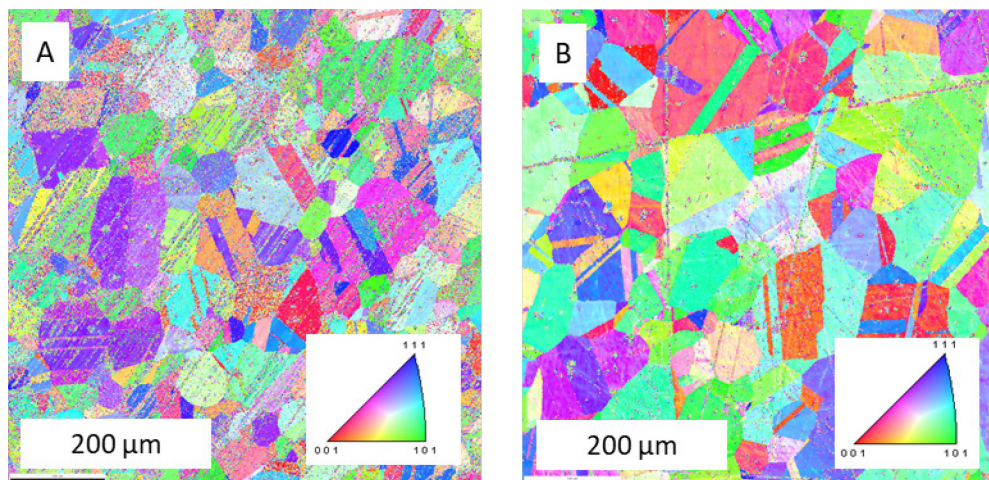


Figure 6. EBSD image of as-prepared Hastelloy N sample (a) pre-permeation testing and (b) post-permeation testing.

A Perkin Elmer PHI-660 Scanning Auger Microprobe (SAM) assessed the surface chemistry of the as-prepared Hastelloy N sample. Auger electron spectroscopy (AES) survey scans were taken both pre- and post-depth profiling (DP) from 30 eV to 1000 eV with 200 meV/s scan rate and 10 cycles using a 3 kV electron beam energy, shown in Figure 7. All major elements of Hastelloy N were identified (Ni, Mo, Cr, and Fe). The pre-DP scan showed significant O and C on the surface. The C peak is indicative of adventitious C, rather than carbide C. Both C and O were nominally removed during depth profiling.

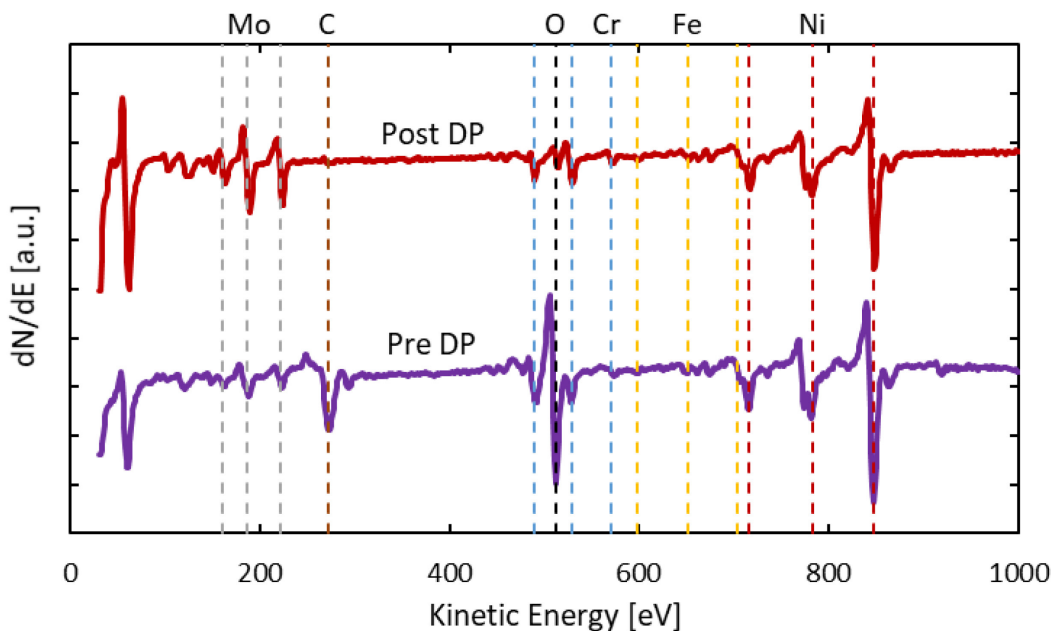


Figure 7. AES survey scans pre- and post-DP with 3 kV electrons. Major elements are labelled at the top.

The depth profile scans used 3 keV Ar ions at 10 mPa and 25 mA producing an ion flux of  $6.6 \times 10^{18}$  ion  $\text{m}^{-2} \text{s}^{-1}$ . The depth profile used a total of five cycles of 60 s sputtering, shown in Figure 8. Oxygen and carbon were both removed to background levels upon the first sputtering cycle, indicating these elements were present on the surface as a monolayer or surface-adsorbed species rather in a layer of oxide or carbide several monolayers thick. The small background presence of oxygen in the sample may indicate

$\text{Cr}_2\text{O}_3$  persisted beyond the surface but determining the exact speciation of metal oxides is challenging with AES measurements.

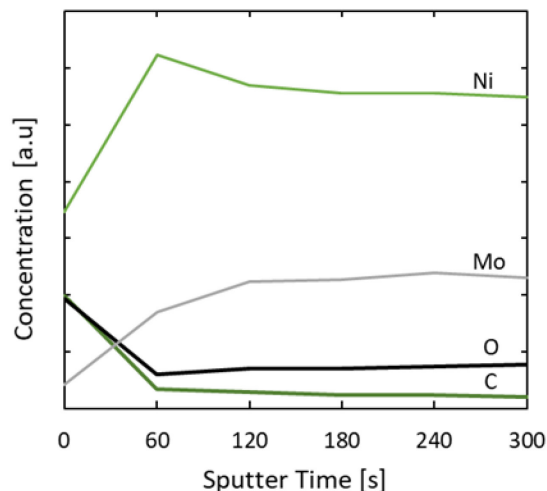


Figure 8. AES depth profile of Hastelloy N.

The Ar sputtering conducted during the depth profile etched the sample to reveal the microstructure, and an SEM image, Figure 9, was also taken by SAM upon completion of AES scans. This image is in good agreement with those taken by EBSD.

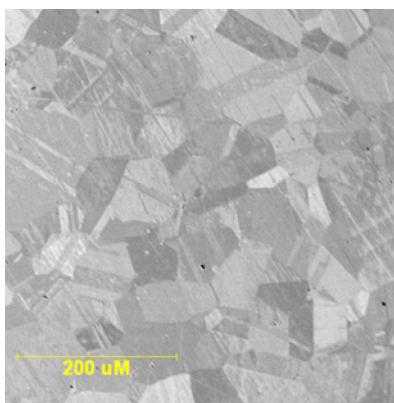


Figure 9. SEM images taken post sputtering at 3kV.

### 3.2 Permeation Apparatus

The imaged and analyzed Hastelloy N sample was washed with acetone followed by ethanol and then installed into the Static Gas Absorption and Permeation (SGAP) apparatus at the INL STAR facility (see SGAP photo in Figure 10). The sample was sealed with two 20 mm outer diameter (OD) Inconel CSI (Centering Ring, Sealing Element, Inner Ring) rings compressed between the 316 stainless-steel housing shown in Figure 11. The compressed CSI ring inner diameters (ID) were 16.4 mm and measured post-test; this was used to calculate the effective permeation surface area. The sample housing was inserted into a quartz tube surrounded by a tube furnace and sealed with quick connect O-ring couplings. A K-type thermocouple is then inserted into the primary side until it is in contact with the primary side sample surface. This thermocouple controls the tube furnace temperature and over-temperature features.





Figure 10. Photo of the SGAP apparatus at INL.

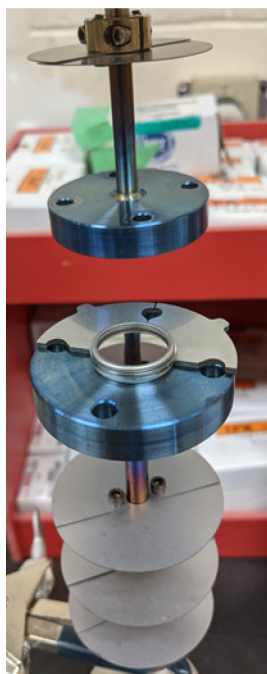


Figure 11. Sample sealing and housing in SGAP.

The quartz tube surrounding the sample housing was rough pumped to a pressure of  $\sim 1$  Pa. The primary and secondary sides of the sample were evacuated with two turbo-molecular pumps connected to each side until base pressure of  $< 10^{-5}$  Pa was reached. Prior to the permeation campaign, the test section was heated to  $500^{\circ}\text{C}$  for four hours and then was exposed to permeating  $\text{D}_2$  for another four hours. This procedure baked-out and facilitated the removal of water, carbon, and protium species in the sample, housing, and vacuum lines.

Permeation experiments were conducted using the following procedure. The sample was heated to the desired temperature. The temperatures investigated in this campaign were 500, 565, 600, 650, and  $700^{\circ}\text{C}$ . Once the temperature stabilized at the desired value ( $\pm 0.5^{\circ}\text{C}$ ), the filament of a MKS eVision 2 Residual Gas Analyzer (RGA) was turned on and commenced scanning the continuously evacuated secondary side. The RGA signals reached a steady-state value between 10–120 min depending on the condition of the vacuum, and these values were taken as the initial background levels.

The first set of permeation data were acquired by first expanding deuterium gas (Advanced Specialty Gases, UHP 5 N) into the primary side to reach the desired testing pressure. The primary side pressure is

recorded with 1000, 30, and 1 Torr MKS baratrons. The permeating D species were recorded with the RGA until steady-state values in the RGA signal were observed. This method is called the “pressure rise” method. Once steady-state was achieved, a pneumatic-controlled valve was closed to isolate the secondary side from the pump train and RGA. The pressure in the isolated volume increased with respect to time as D<sub>2</sub> permeated through the sample. This pressure was measured with 0.02, 10, and 1000 Torr MKS baratrons and recorded with an interfaced LabVIEW VI. This test is called the “buildup” method and provided a second and direct measurement of the permeation rate. After 120–300 s of measuring the buildup pressure, the isolation valve was reopened and the RGA signal was allowed to reach steady-state once again. The primary side was then evacuated, and the RGA signal declined to a background level. This method is called the “evolution” method. Detailed discussion on the analysis of these three methods is provided in the subsequent section.

The first campaign was performed with deuterium which provided better sensitivity with the RGA. Multiple pressures were tested at each temperature. A greater number of pressures were tested at 565°C and 650°C due to their relevance to MSRE tritium transport analysis. An attempt was made to probe into the surface-limited regime by testing pressures down to 100 Pa at 565°C and 13 Pa at 650°C. A second campaign was performed with hydrogen at 500, 565, 600, 650, and 700°C but only at an applied pressure of 10 kPa.

### 3.3 Permeation Theory and Analysis

The buildup method, described above, provides a direct measurement of the permeation rate. The relation between pressure increase measured with the baratrons and permeating flow rate is described by:

$$J = \frac{V}{A R T_{\text{gas}}} \frac{dP}{dt} \quad (14)$$

Ideal gas behavior is assumed, which is validated by the very low-partial pressures of D<sub>2</sub> at nominally room temperature. The molar flux (J) is calculated from the isolated and calibrated volume (V), the gas temperature (T<sub>gas</sub>), gas constant (R), sample surface area (A), and the first derivative of pressure with respect to time (dP/dt). The permeability can then be calculated using the relation in Equation (6).

The diffusivity (D) is obtained from the transient data collected in the pressure rise and evolution method. Calculating diffusivity originates with Fick’s 2nd law:

$$\frac{\partial C}{\partial t} = D \frac{\partial^2 C}{\partial x^2} \quad (15)$$

For the pressure rise method, the following boundary conditions are applied to solve for the analytical solution of Equation (15):

1.  $C(t \leq 0, x) = 0$
2.  $C(t, x = x_2) = 0$
3.  $C(t > 0, x = x_1) = C_1$

The subscripts 1 and 2 indicate the primary side and secondary side of the SGAP apparatus, respectively. Physically, the boundary conditions state that the sample is initially evacuated, so the hydrogen concentration is nominally zero. At all times, the secondary side is continuously evacuated, so the concentration on the secondary side surface is nominally zero. At  $t = 0$ , a pressure is introduced to the sample so the concentration on the primary side surface is fixed to a value ( $C_1$ ) in equilibrium with the gas-phase pressure at  $t > 0$ . The analytical solution of Fick’s 2nd law with the above boundary conditions simplifies when it is normalized with the steady-state permeation rate. A nonlinear least squares



regression (NLSR) method is used to solve for the diffusivity,  $D$ , by fitting the experimental data to the analytical solution:

$$\frac{J(t)}{J_{ss}} = 1 + 2 \sum_{n=1}^{\infty} (-1)^n \exp\left(-\frac{Dn^2\pi^2}{l^2}t\right) \quad (16)$$

The diffusivity can also be obtained by solving the analytical solution Equation (16) at a fixed ratio. For example, Louthan and Derrick [18] use the following:

$$\frac{J(t^*)}{J_{ss}} = 0.900 \quad \frac{Dt^*}{l^2} = 0.312 \quad (17)$$

Using this method, the characteristic time ( $t^*$ ) is found to satisfy the specified ratio, and diffusivity is subsequently calculated. In this work, the characteristic time method is also used to provide an initial guess for the NLSR solving.

The evolution method provided a second set of transient data to solve for diffusivity. For this method the boundary conditions to solve Fick's 2nd law are:

4.  $C(t \leq 0, x_1) = C_1$
5.  $C(t, x = x_2) = 0$
6.  $C(t > 0, x = x_1) = 0$

For the evolution method, the primary surface is initially at a fixed concentration ( $C_1$ ) in equilibrium with the gas-phase pressure in the primary side, while the secondary surface is continuously evacuated resulting in a concentration that is nominally zero. At  $t = 0$ , the primary surface is evacuated causing the concentration at the primary surface to be zero at  $t > 0$ . The resulting normalized analytical solution is:

$$\frac{J(t)}{J_{ss}} = -2 \sum_{n=1}^{\infty} (-1)^n \exp\left(-\frac{Dn^2\pi^2}{l^2}t\right) \quad (18)$$

As with the rise method, the diffusivity can also be obtained by solving the analytical solution of Equation (18) at a fixed ratio. Louthan and Derrick [18] use the following for the evolution method:

$$\frac{J(t)}{J_{ss}} = 0.450 \quad \frac{Dt}{l^2} = 0.150 \quad (19)$$

Here the steady-state permeation is defined for  $t < 0$ , prior to evacuating the primary side.

Yamanishi et al. [19] suggest the evolution method is superior to the rise method for diffusivity measurements. The hydrogen permeation experiment may clean the surfaces, and therefore, the measurement is not impacted by transients induced by removal surface absorbed species. Our campaign confirmed this statement as the evolution method resulted in higher accuracy in model fits compared to the rise method.

### 3.4 Permeation Results

The clean Hastelloy N molar fluxes taken from the buildup method are reported in Figure 12. The fluxes were calculated from Equation (14). Power-law models were fit to the flux-pressure data to obtain the Sieverts' constant ( $n$ ) which are reported next to the temperature legend. At each temperature, the

optimized value of  $n$  was nominally 0.5. This indicates the transport was limited by interstitial diffusion through the metal. Whereas, if surface reactions were rate-controlling, a pressure dependence  $\sim P^1$  would be observed.

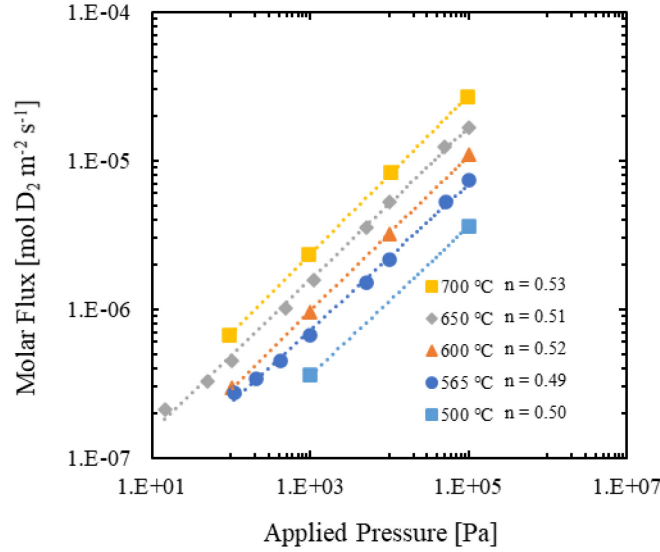


Figure 12.  $D_2$  flux vs. pressure from the buildup method.

Diffusivity was calculated at each pressure and temperature using the transient data collected in the rise method, and the values are reported in Figure 13. The diffusivities calculated from the evolution method are shown in Figure 14. While the diffusivities calculated by both the characteristic time and NLSR are comparable for both the rise and evolution methods, the agreement between the characteristic time and NLSR is better for the evolution method. However, the pressure dependence observed with the evolution method may result from interactions with the heated structural material as an environmental effect rather than physical phenomena of the diffusivity through Hastelloy N. Further experiments are required to deconvolute this observation.

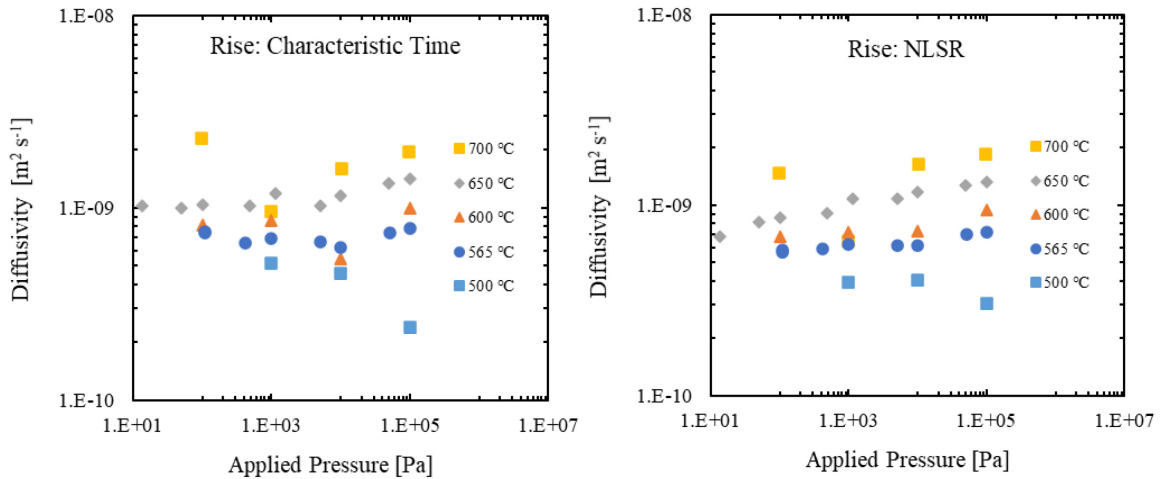


Figure 13. Diffusivity from the rise method calculated from characteristic time (left) and NLSR fitting (right).

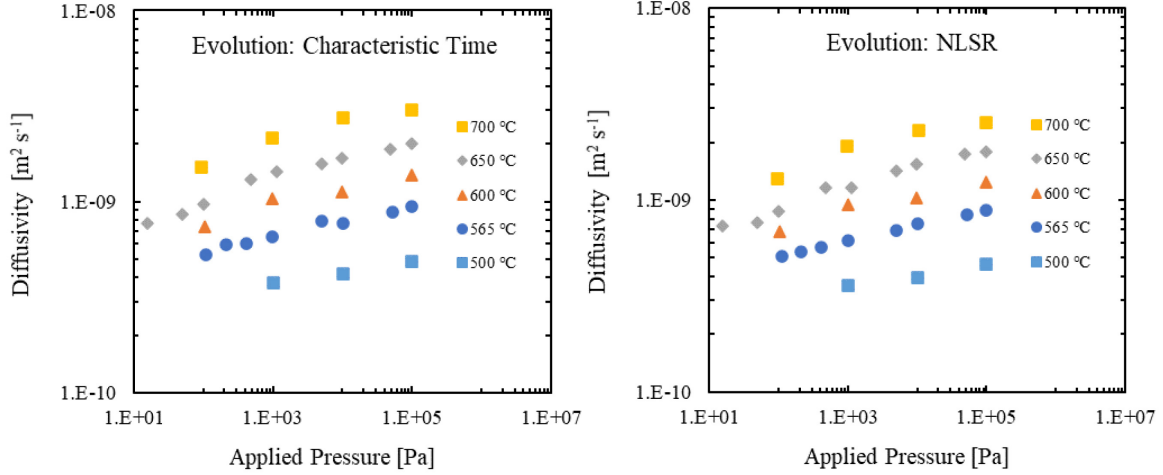


Figure 14. Diffusivity from the evolution method calculated from characteristic time (left) and NLSR fitting (right).

Arrhenius models were applied to permeability and diffusivity data at 10 kPa to compare both  $D_2$  and  $H_2$ . Solubility was calculated by the relation  $\Phi = DK_S$ . The permeability measured in this campaign by the buildup method compares well with the measurement by Zhang et al. [20], as shown in Figure 15. Note the same supplier, Haynes International Inc., produced the Hastelloy N for both studies. The permeability is slightly greater than that measured by Webb [21] and comparable with that measured by Strehlow and Savage [22]. The fitted permeability models for hydrogen and deuterium are reported below, respectively.

$$\Phi_H = 5.81 \pm 0.58 \times 10^{-7} [\text{mol m}^{-1} \text{s}^{-1} \text{Pa}^{-0.5}] \exp\left(\frac{-66.3 \pm 0.68 [\text{kJ mol}^{-1}]}{RT}\right) \quad (20)$$

$$\Phi_D = 2.40 \pm 0.70 \times 10^{-7} [\text{mol m}^{-1} \text{s}^{-1} \text{Pa}^{-0.5}] \exp\left(\frac{-62.2 \pm 1.8 [\text{kJ mol}^{-1}]}{RT}\right) \quad (21)$$

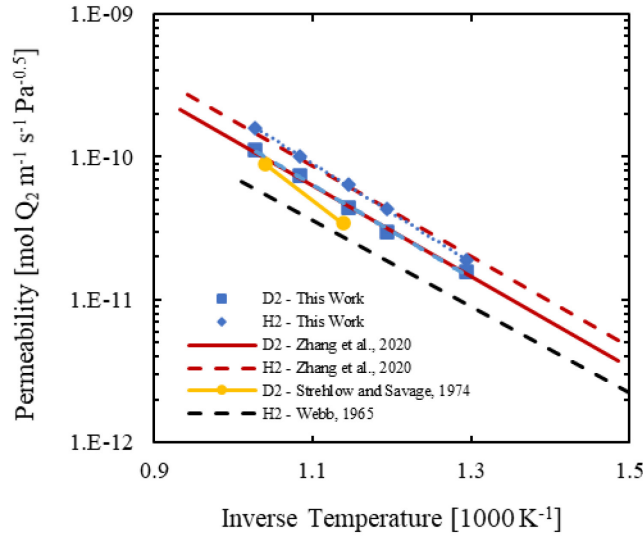


Figure 15. Arrhenius plot of hydrogen isotope permeability in Hastelloy N and literature comparisons [20-22].

The diffusivity at 10 kPa is reported in Figure 16 for both hydrogen and deuterium using the evolution NLSR values. The diffusivity values are lower than those reported by Zhang et al. [20] in the comparable temperature range. The activation energy of diffusion is also greater than previously reported. While permeability is a steady-state measurement, diffusivity is a transient measurement and differences in measurement techniques and apparatus have a greater effect on the calculated diffusivity. Zhang et al. [20] used a transient buildup method and calculated diffusivity from the characteristic time lag. The fitted diffusivity model from the data measured in this campaign for hydrogen and deuterium are:

$$D_H = 2.93 \pm 0.72 \times 10^{-6} [\text{m}^2 \text{s}^{-1}] \exp\left(\frac{-56.0 \pm 1.6 [\text{kJ mol}^{-1}]}{RT}\right) \quad (22)$$

$$D_D = 1.96 \pm 0.25 \times 10^{-6} [\text{m}^2 \text{s}^{-1}] \exp\left(\frac{-54.8 \pm 0.8 [\text{kJ mol}^{-1}]}{RT}\right) \quad (23)$$

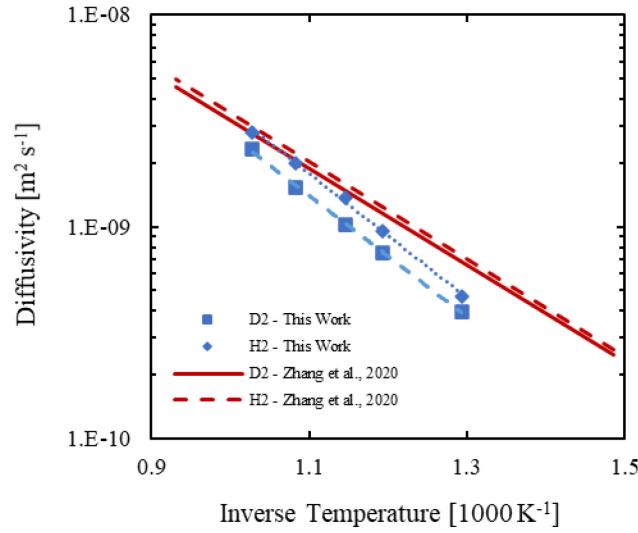


Figure 16. Arrhenius plot of hydrogen isotope diffusivity in Hastelloy N.

The calculated solubility values are reported in Figure 17, and the fitted results for hydrogen and deuterium are below:

$$K_{S,H} = 0.20 \pm 0.03 [\text{mol m}^{-3} \text{Pa}^{-0.5}] \exp\left(\frac{-10.3 \pm 1.1 [\text{kJ mol}^{-1}]}{RT}\right) \quad (24)$$

$$K_{S,D} = 0.12 \pm 0.03 [\text{mol m}^{-3} \text{Pa}^{-0.5}] \exp\left(\frac{-7.5 \pm 1.7 [\text{kJ mol}^{-1}]}{RT}\right) \quad (25)$$

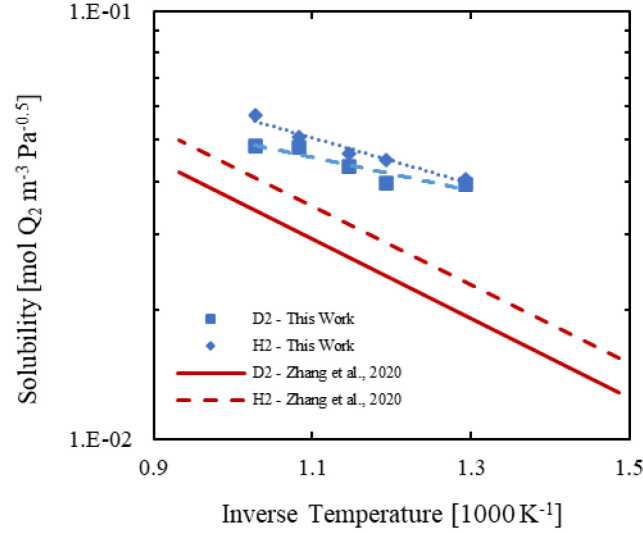


Figure 17. Arrhenius plot of hydrogen isotope solubility in Hastelloy N.

The permeation campaign attempted to measure surface kinetic constants for clean Hastelloy N. However, no surface effects were observed within the operational limits of the apparatus (100 Pa at 565°C and 13 Pa at 650°C). Surface effects would be noticed in Figure 12 by a flux-pressure dependence of  $J \sim P^1$  in the limit of low pressures, yet, the observed flux-pressure dependence remained  $J \sim P^{0.5}$ . Since the diffusion-limited transport regime was maintained at the lower pressure limit of our measurements, we can assume the permeation number  $W$  was much greater than one (say, 95) in these cases and use this to bound the values of  $k_d$  and  $k_r$ . Assuming  $W \geq 95$ , the bounds on  $k_d$  calculated from Equation (7) are:

$$\begin{aligned} k_d(565^\circ\text{C}) &\geq 2.2 \times 10^{-7} \text{ mol m}^{-2} \text{ s}^{-1} \text{ Pa}^{-1} \\ k_d(650^\circ\text{C}) &\geq 1.4 \times 10^{-6} \text{ mol m}^{-2} \text{ s}^{-1} \text{ Pa}^{-1} \end{aligned} \quad (26)$$

These values fall in the high end of the range of values measured for other high-nickel superalloys as shown in Figure 18 and are similar to those reported for clean Inconel 625 [15].

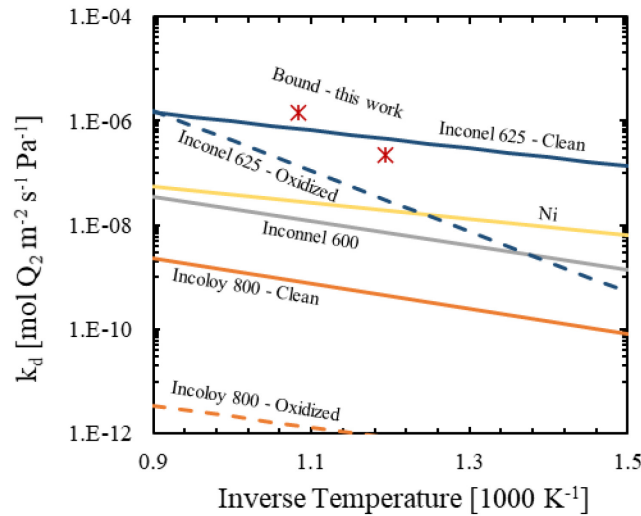


Figure 18. Dissociation rate constant  $k_d$ , for select metals included in Table 3 as well as the lower bound values for Hastelloy N from this study.

We plan to conduct a second campaign with a thinner (0.1–0.2 mm) clean Hastelloy N sample to better probe surface rate constants within the capabilities of the SGAP apparatus. A thinner membrane lowers the value of the permeation number  $W$ , thereby making the surface-limited regime accessible at higher pressures. A third campaign will be conducted on oxidized Hastelloy N to understand the difference in hydrogen transport parameters due to the formation of thick  $\text{Cr}_2\text{O}_3$  layers.

## 4. The Molten-Salt Tritium Transport Experiment

This section describes the Molten-Salt Tritium Transport Experiment (MSTTE, pronounced “misty”), a forced convection salt loop to study combined effects tritium transport phenomena of the salt-metal system under relevant MSR conditions. First, an overview of MSTTE is presented followed by a detailed description of each component. This experiment can also be modified for future campaigns investing bubble transport and graphite interaction.

### 4.1 Experiment Overview

The scope of MSTTE is to study tritium transport for the salt-structural material system in a forced convection FLiBe loop specifically targeting tritium transport in several transport limited regimes: diffusion, surface reaction, and salt-phase mass transport. Hydrogen isotopes will be injected into the flowing salt stream, then removed through a thin-walled test section representative of MSR structural materials: Hastelloy N, SS 316, etc. Data collected from this campaign will be used to validate tritium transport models and codes for the safety and licensing analysis performed for future MSRs.

We will conduct the MSTTE campaign in a phased approach. Phase I is non-radiological, and the permeating gas species will be deuterium. This will allow a faster shake down of experiment operation and provide an initial data set for transport analysis. Phase II introduces tritium into the system which will allow for high measurement sensitivity and representative data sets for tritium transport.

In each phase, a campaign will be performed on both a “clean” and “oxidized” sample. The “clean” sample will be mechanically and chemically polished to remove surface oxide species, and the “oxidized” specimen will be first mechanically and chemically polished, but then exposed to a set partial pressure of oxygen at elevated temperature to develop an oxide layer on both surfaces. The “clean” specimen is most representative of the salt-metal-salt applications (i.e., heat exchanger tubes), where both surfaces are expected to be clean by contact and reduction by the salt. The oxidized specimen is anticipated to represent the salt-metal-air system (i.e., reactor vessel, heat exchanger shell, and structural piping), where over time the outer surface is oxidized from contact with air while the metal is at elevated operating temperatures.

The experiment’s design is versatile to accommodate future campaigns for other transport phenomena (e.g., bubble flow or graphite interactions). This is achieved by a redesign and exchange of the test section and gas distribution system.

The piping and instrumentation diagram (P&ID) of MSTTE is shown in Figure 19. The primary systems of the experiment include:

- Test section
- Permeated gas analysis system
- Plenum/redox control
- Reverse permeator
- Molten-salt pump
- Flow meter and pressure gauge
- Fill/dump tank

Table 5 lists the primary equipment needed for this study. Hastelloy N is presently identified as the default wetted component material; however, this may be changed to 316 SS if the latter is deemed a better representation of candidate structural material for current MSR designs, and corrosion is not a significant concern.

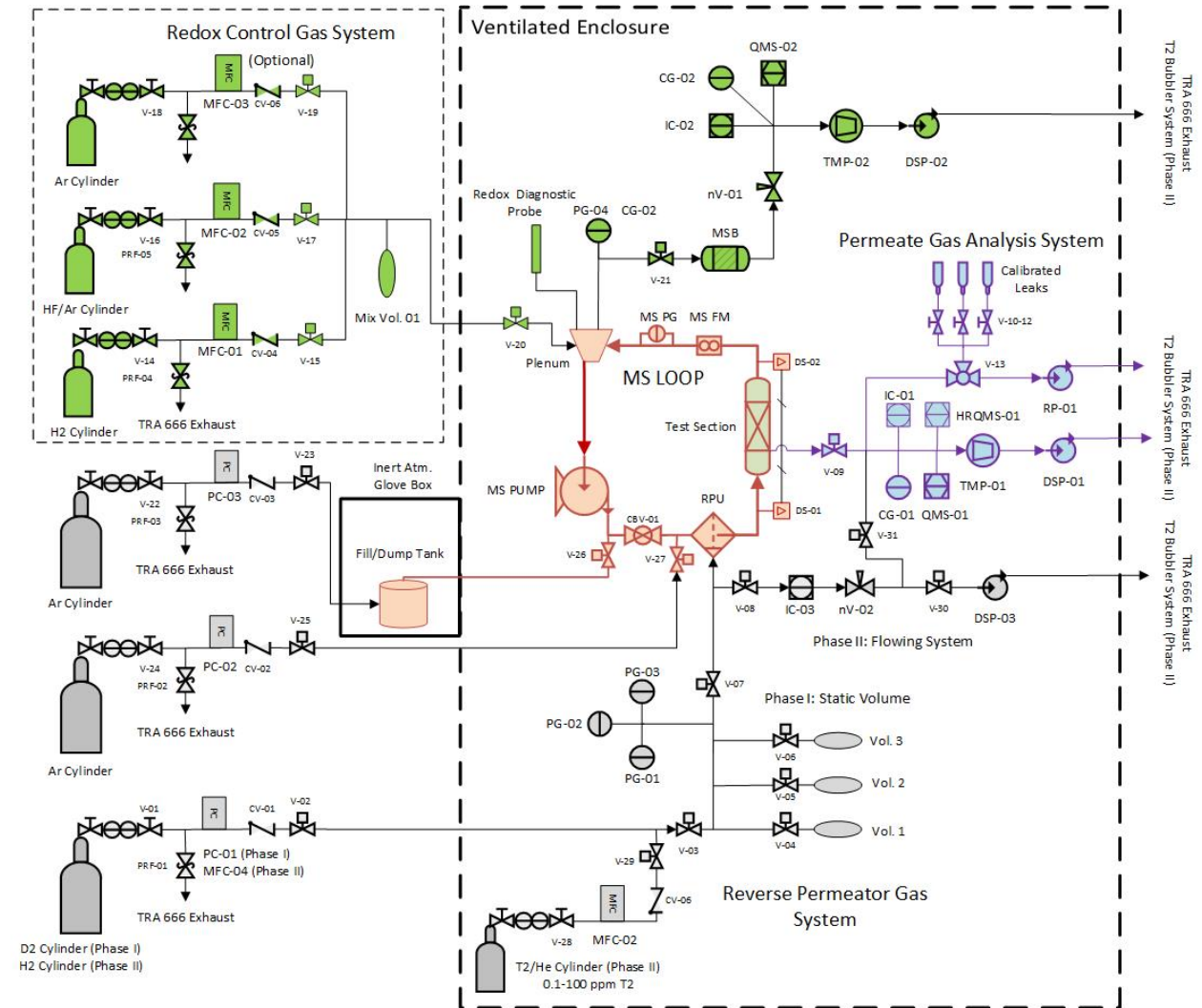


Figure 19. Piping and instrumentation diagram of the test loop (MSTTE). Grey indicates the gas distribution system (1/4" VCR fittings), blue indicates the permeate gas analysis system (also 1/4" VCR and CF-flange components), red indicates the molten-salt loop (1" Swagelok fittings), and green indicates the redox/plenum gas system (1/4" VCR and CF-flange components).

Table 5. Major equipment table including symbols, manufacturer, and product number for MSTTE.

Symbol	Equipment	Manufacturer	Product Number	Quantity
PC-01	Downstream Pressure Controller D <sub>2</sub> – 2000 Torr – 1000 sccm	MKS	GPCA23TR2D	1
PC-02&03	Downstream Pressure Controller Ar – 100 psia – 10000 sccm	MKS	GPCA12PR4D	2

PC-04&05	Downstream Pressure Controller H <sub>2</sub> and HF/Ar	MKS	GPCA12PR4D	2
MFC	Mass Flow Controller	MKS	GM50A013101RMM020	4
V	¼" VCR Pneumatic Valve SS 300 Series, Vespel Tip	Swagelok	SS-4BK-V51-VP	20
V	¼" Three-Way Valve	Swagelok	SS-43GXS4	1
V	¼" Manual Valve	Swagelok	SS-4BK	3
CBV	½" Swagelok Molten-Salt Compatible Ball Valve	CeraValve	KST-HT	3
CV	¼" VCR Check Valve	Swagelok	SS-4C-VCR	7
PRF	¼" Swagelok Pressure Relief Valve	Swagelok	SS-RL3S4	6
nV	¼" Swagelok Needle Valve	Swagelok	SS-1RS4	2
	1" Swagelok Hastelloy cross	Swagelok	HC-1630-4	1
	1" Swagelok Hastelloy tee	Swagelok	HC-1630-3	3
	1" Hastelloy tubing	Swagelok	OS-HC-T16-S-083-20	40
	1" Swagelok Hastelloy union	Swagelok	HC-1630-6	5
V	Gas Cylinder Regulator	Mattheson	Various	7
Vol.	Calibrated Control Volume			3
	Calibrated Leak	Laco	Various	3
PG 01-03	Baratron/Capacitance Manometer	MKS	627D-29720	1
			626C11TBE	1
			626C12TBE	1
CG	Combination Gauge	Inficon	BPG 400	3
IC	Ion Chamber	Femto-TECH	U24-D	3
QMS	Quadrupole Mass Spectrometer	MKS	e-Vision2, EVE-120-001	2
HR-QMS	High-Resolution Quadrupole Mass Spectrometer	MKS	Microvision 2, 669-720-031	1
TMP	Turbo-Molecular Pump	Agilent	X3500-64005	2
DSP	Dry-Scroll Pump	Agilent	X3815-64010	3
RP	Mechanical Roughing Pump	Pfeiffer	DUO 5	2
	Glovebox	MBraun	1600871	1
	Experiment Enclosure	Permacon	CS105	1
	Tube Furnace	Mellen	SV10-4.3x12-3Z	1
	Quartz Test Section	Larsen	TBD	1



	Conflat Vacuum Section	Nor-Cal Products	Various	1
	Plenum	Nor-Cal Products	TBD	1
	Fill/Dump Tank	GANDF	TBD	1
RDP	Redox-Diagnostic Probe			
RPU	Reverse Permeator Unit	Nor-Cal	TEX FRP v1	1
DS	Differential Gas Sensor		Custom	1
MS FM	Molten-Salt Flow Meter	FLEXIM	WI-400MDST012CMZ	1
MS PG	Molten-Salt Pressure Gauge	Creative Engineers, Inc.	TBD	1
MS Pump	Molten-Salt Pump	Nagle Pumps, Inc.	C1-05-010	1
TC	Thermocouple	AccuGlass	100967	80
	Heat Tape	Omega	DHT051020LD	20
	Heat Tape Power Supply System	Tempco		1
	Instrumentation and Control System	NI		1
	Fire suppression	StatX		
	Exhaust HEPA Filters			
	Exhaust Getter Beds			
	FLiBe	U.Wisc		
	Tritium Gas	SRNL		

## 4.2 Major Equipment/Components

### 4.2.1 Test Section

The test section consists of a tube (Hastelloy N, 316 SS, or any other alloy of interest) with an ID of 8 mm, wall thickness of 0.5 mm, and length of 15 cm. This test section meets MSR-relevant transport regimes with reasonable experimental conditions (see Section 4.4 for greater detail). This tube will be welded to 1-inch seamless tubes of an identical material. This test section will be inserted into a quartz tube with quartz-to-metal transitions and CF flanges for high-vacuum compatibility. The test section will be connected to the remainder of the salt-loop plumbing with commercial Swagelok fittings. These connections will be inside CF-flange vacuum compatible cubes to enable connection and disconnection of the test section to the loop. The bottom cube is attached to the quartz tube via bellows for ease of assembly. See Figure 20 for an example test section used in the PreTEX (Pre-Tritium Extraction Experiment) apparatus at INL.

The quartz tube is then housed inside a clam-shell tube furnace with a 12-inch heated zone. Salt flows inside the tube and the dissolved D/T permeates through the test section into a volume contained by the quartz tube and continuously evacuated by the permeate gas analysis system.

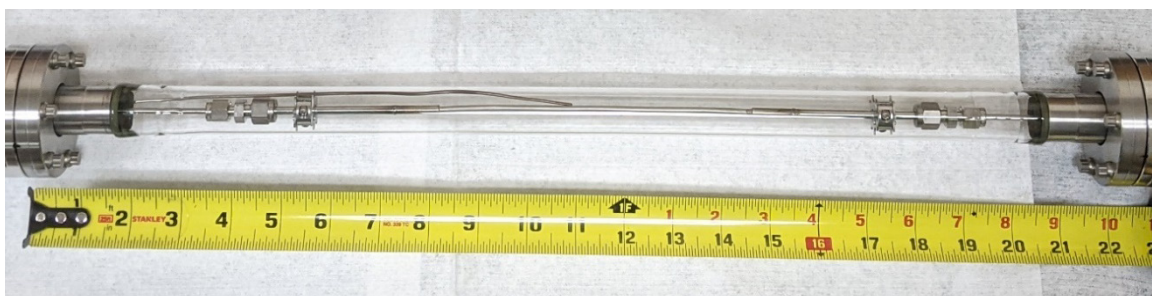


Figure 20. Example of similar test section used in the PreTEX experiment at INL.

#### 4.2.2 Permeate Gas Analysis System

The secondary side of the test section is evacuated with a turbomolecular pump roughed by a dry scroll pump. Dry scroll pumps are superior for tritium applications as they do not expose the pumped gas species to organic lubricants or oils that undergo exchange reactions and trap the tritium. Two quadrupole mass spectrometers (QMS) and an ion chamber (for Phase II tritium) measure the hydrogen isotope permeation rates. The QMSs enable speciation as well as a quantitative flow rate measurement. One QMS is a 1–100 amu mass-range instrument to measure vacuum impurities such as water and carbon compounds. One is a high-resolution 1–6 amu instrument, specifically tailored for speciation of the hydrogen isotopes. The QMSs are calibrated prior to each campaign with a bank of calibrated leaks allowing for conversion of QMS signal to flow rate. The ion chamber is a highly sensitive radiation detector for tritium concentration measurements. The ion chamber is calibrated with a gamma source prior to tritium permeation measurements.

#### 4.2.3 Plenum

The plenum component has three purposes: (1) fluid level sensing for introducing salt into the loop; (2) provide a free surface and volume for fluid expansion and contraction as the salt is heated/cooled; (3) provide space for the optional diagnostics and redox control.

A calibrated thermocouple array is inserted into the plenum region which acts as a fluid level sensor for introducing salt into the loop and during experiments. As salt contacts a thermocouple, an increase in temperature is recorded and fluid level known. The density of the salt changes with temperature, and therefore, a free surface/volume is required to allow for this expansion and contraction with temperature.

As discussed in our previous report [1], the salt chemistry influences tritium speciation, and hence tritium permeation. In a reactor environment, tritium may be present as either TF or T<sub>2</sub>, and the redox chemistry of the salt determines their ratio. It is assumed only tritium in the form of T<sub>2</sub> permeates. In order to limit the present experiment's cost and complexity, we have chosen to focus initially on clean salt and transport and permeation of T<sub>2</sub> only, without any specific investigation of the chemistry that would require the introduction of HF. Should future campaigns require this, however, it can be achieved in the plenum region as proposed in the design by Rader et al. [23], in which three separate cylinders are connected via mass flow controllers to a mixing volume. A controlled amount of each gas can be introduced into the plenum region and absorb into the flowing salt. The mixture's pressure is controlled with a needle valve (nV-01), and redox-control gases can be introduced to meet required potentials. A redox diagnostic probe would need to be procured from a strategic partner in the MSR program in order to measure the fluorine potential in the salt in the event such a campaign is ultimately pursued.

#### 4.2.4 Reverse Permeator Unit

In an out-of-pile experiment such as this, an artificial means of introducing tritium into the salt loop is required. Of the various methods (bubbling, LiT, and reverse permeator) discussed in our previous report [1], the reverse permeator was chosen as the best introduction method as tritium is uniformly permeated into the salt with a controlled and measured rate.

The reverse permeator is also planned for the Tritium Extraction Experiment (TEX) at the STAR facility to test tritium extraction from the liquid metal eutectic, Pb-17Li. Figure 21 shows a drawing of the reverse permeator unit and a picture of the fabricated component for the TEX experiment. In this design, four closed-end permeator tubes are inserted into an expansion chamber. FLiBe will flow through the expansion chamber and hydrogen ( $D_2$ ,  $H_2 + HT$ ) will be introduced inside the permeator tubes. The hydrogen species diffuse through the permeator tubes and into the flowing FLiBe stream. For MSTTE, thin-walled pure Ni can be used as the permeator tube material.

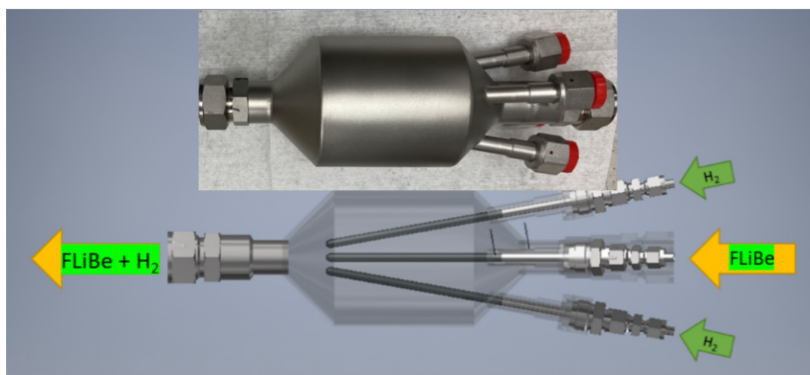


Figure 21. Reverse permeator design.

In Phase I, the non-radiological deuterium phase, the pure  $D_2$  gas is introduced to closed-end permeator tubes with a pressure controller. The valves V-03 and V-08 isolate the component to a calibrated volume, and the pressure gauges/baratrons (PG-01-03) measure the pressure drop with time to calculate a permeation rate. V-02 and V-03 are opened periodically to replenish the  $D_2$  in the calibrated volume(s). V-08 is opened to evacuate the reverse permeator with DSP-03. Three calibrated volumes (Vol.1–3) are attached to change the static volume size to accommodate a range of permeation rates.

In Phase II, the tritium phase, a cylinder containing a known amount of tritium (0.1–100 ppm) diluted in He is mixed with  $H_2$  and introduced to the reverse permeator unit. A flowing system is implemented to prevent reduction in HT partial pressure. The applied pressure is controlled by adjusting a needle valve (nV-02). An ion chamber (IC-03) measures the amount of tritium remaining downstream of the reverse permeator and enables us to calculate the amount of tritium introduced to the salt. Ion chamber (IC-01) records the amount of tritium permeating through the test section. IC-02 records the amount of tritium evolving in the plenum region. We can also measure the amount of tritium permeating through the loop structural piping by recording the amount of tritium in the engineered enclosure's exhaust (an activity already in practice at the STAR facility). This design is similar to the Tritium Gas Absorption and Permeation (TGAP) apparatus in operation at the STAR facility [24, 25].

#### 4.2.5 Molten-Salt Pump

Centrifugal pumps are the most common pump used in forced convection salt loops. Here we identify two pumps used in similar loop design. The Oak Ridge National Laboratory (ORNL) FLiNaK loop uses a custom-built centrifugal sump-type pump with overhung impeller. The pump volute, impeller, and top plate were custom designed and machined from Inconel 600. A John Crane-type 2800 rotating shaft seal isolates the sump tank Ar cover gas from atmosphere. The shaft is connected to a 10-HP Brook Crompton

motor with a Lovejoy drive shaft. This design is capable of supplying 0.125 MPa head at 4.5 kg/s and a maximum head of 7.4 m [26]. The University of Wisconsin-Madison (UW-M) forced-convection nitrate-salt heat transfer loop uses a commercial Nagle 1.5-in.  $\times$  2-in. CWO-RS frame 95, at a 3-ft setting, Serial No. A8-1245, vertical cantilevered shaft pump made of 316 SS. This pump is reported to produce a maximum limit 450 lpm at 4.6 m pump head for the UW-M loop [27]. The same Nagle pump will be used in this loop design and will provide 25-feet head pressure. Section 4.4.1 shows these pumps achieve relevant flow rates for our loop design.

#### **4.2.6 Flow Meter and Pressure Gauge**

Several options for measuring flow in the FLiBe are available, including commercial products. The Flexim WaveInjector flow meter is a non-invasive ultrasonic flow transducer compatible to temperatures as high as 600°C. It is installed on the outside surface of the flow tube and does not introduce a pressure drop into the system. This flow meter has been investigated in previous molten-salt loops, and its use was described previously [26].

High-temperature pressure transducers are necessary to measure the pressure of the FLiBe in the loop. Traditional pressure gauges are not suitable for use in molten FLiBe primarily due to the high-temperature requirements and material compatibility. A suitable pressure transducer for FLiBe is found in a diaphragm connected to a pressure gauge via a remote capillary. This product is supplied by Creative Engineers Inc. and is filled with NaK. Compared to other remote diaphragm gauges that may be filled with an organic medium, this liquid metal-filled pressure transducer has an outstanding temperature range where it maintains its liquid state at room temperature and can be used at temperatures as high as 815°C.

#### **4.2.7 Supply Tank**

Loading and unloading of the loop requires a supply tank to store the initial volume of salt that will occupy the loop. The loop will be initially filled by first evacuating the loop using a turbomolecular pump and then filling the loop from the supply tank using pressurized inert gas. Given the needed pressures and the dimensional requirements of the supply tank, this requires it be rated as a pressure vessel. A supply tank has been designed to ASME Section VIII, Division 1 that will be used to perform the initial melt, fill the loop, and serve as a drain tank for emptying the loop in normal and off-normal situations. The supply tank will be contained in a glovebox in order to protect personnel during loading procedures and maintain purity of the salt. Purified FLiBe will be purchased and used in this experiment. This eliminates the need for an online purification process.

The supply tank will include a thermocouple array to determine the height of the molten FLiBe. A head flange will be included that connects this array in addition to a series of valves to allow for the introduction of and pressurization with inert gas. A valve on the bottom of the tank will be opened to allow molten FLiBe to leave the supply tank and fill the loop. The loop can be drained using the same valve. A redundant emergency drain is located at the top of the supply tank that will not otherwise be used. The supply tank design is shown in Figure 22.

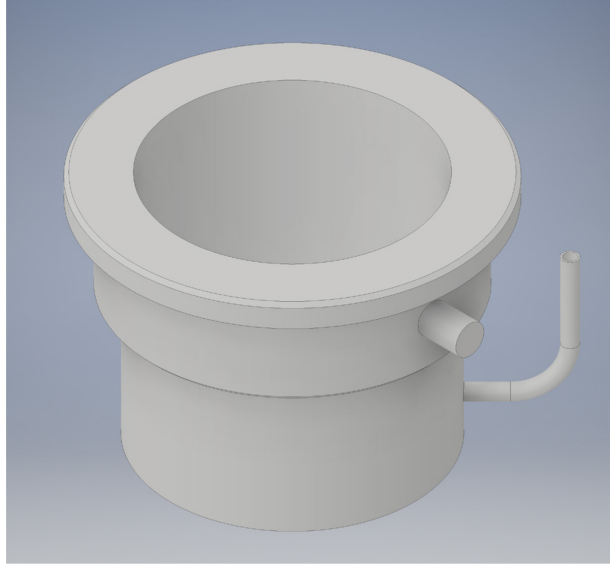


Figure 22. FLiBe supply tank.

#### 4.2.8 Differential Gas Sensor

The Fusion Safety Program is working to develop a tritium sensor for use in the PbLi TEX loop. Similar concepts can be extended to the MSTTE loop; however, this is an active area of research and development, and at this time, we do not have a product to install. The following describes the current effort.

A systematic analysis of the hydrogen flow rates entering and leaving the system with respect to time can provide some insight into solubility; however, this analysis is also affected by the entirety of the transport process. The solubility measurements of hydrogen in FLiBe span more than 1000×, which makes differentiation in analysis challenging. Online measurements to provide a qualitative assessment of the concentration as well as the extraction efficiency ( $\eta$ ) reduces the degrees of freedom, allowing for better assessment of experimental data.

The use of a differential sensor removes the uncertainty in the solubility constants when analyzing the test section hydrogen removal, as well as provides a qualitative assessment of solubility when individual measurements are analyzed. This is demonstrated in Equation (27), and a schematic of this sensor design is provided in Figure 23.

$$\eta = \frac{C_{up} - C_{down}}{C_{up}} = \frac{K_H P_{up} - K_H P_{down}}{K_H P_{down}} = 1 - \frac{P_{down}}{P_{up}} \quad (27)$$

Online measurements of hydrogen dissolved in a liquid system make use of gas-liquid equilibrium. Hydrogen is evolved from the liquid, and the quantity is measured in the gas phase. There are three methods to do so:

- Permeation windows
- Porous membranes
- Electrochemical measurements

Permeation windows make use of interstitial diffusion of hydrogen atoms through dense metals. The MELODIE loop [28] provides an example of permeation windows as a tritium sensor in a forced convection loop, albeit for PbLi rather than FLiBe. In the case of FLiBe, a thin-walled pure Ni membrane can be used. Permeation windows only allow transport of hydrogen isotopes and therefore can be used in a closed-ended scheme. Here, a volume is evacuated and isolated. A vacuum ion gauge combined with baratrons measure the resultant pressure increase in the isolated chamber from hydrogen permeation through the window. The steady-state pressure is indicative of the concentration of hydrogen in the salt, related by Equation (3). However, this method only works for hydrogen and does not provide speciation of the different isotopologues. An alternative concept is to continuously evacuate each window and monitor the permeation with QMSs, similar to the permeated gas analysis. With identical pump conductance in each sensor, the QMS signal can be used for the differential analysis. This method provides speciation of the hydrogen isotopes but is a “dynamic” method rather than “equilibrium” method. Therefore, the sensors should be placed in analogous positions for identical fluid velocity profiles in the FLiBe loop, and the vacuum pumping conductance should be identical, enabling direct comparison of the QMS response. The ideal solution is combining two measurements which would provide an equilibrium measurement as well as speciation once the volume is evacuated.

The porous membrane method uses a tuned pore size to prevent the wetting of the fluid but enables the evolution of gases for analysis. The transport resistance through the porous structure is potentially smaller than the permeation window. An example is the membrane gas-liquid contactor (MGLC) investigated for the PbLi system [29]. The Washburn equation describes the equilibrium between capillary pressure and surface tension of the fluid. This equation identifies pore size limits to prevent wetting of the fluid. The pressure of the evolved gas can be measured with the isolated volume method to provide an equilibrium measurement, as well as evacuated and monitored with a QMS, as described above. Note this sensor method is not selective to hydrogen isotopes but would rather provide monitoring of the all dissolved gas species, so speciation is a critical measurement.

The electrochemical measurement uses a high-temperature proton-conducting ceramic to measure the concentration of hydrogen evolved in the gas-phase. This sensor does not have speciation capability of hydrogen isotopes, but the HYCAL probe and analyzer could provide a commercial product solution [30]. The HYCAL system is designed as a hydrogen sensor for molten aluminum alloys, and the operating temperature for 600–800°C would be applicable for higher temperature tests. Further research and development would be required to design and construct a sensor capable of the 500–700°C operating temperatures of MSTTE with FLiBe.

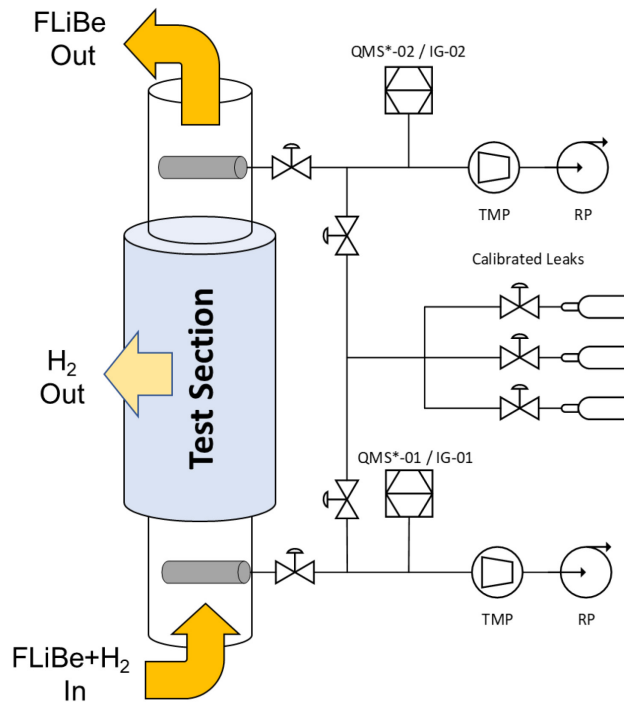


Figure 23. Schematic of the differential gas sensor.

### 4.3 Safety Considerations

The MSTTE apparatus exhibits a number of hazards that must be mitigated and protected against. The loop will be actively heated to temperatures as high as 750°C. Proper insulation, fire suppression, and over-temperature controls will be built into the interlocked experimental control system.

FLiBe carries significant chemical and toxicity concerns, and introducing tritium in Phase II requires special measures to avoid radiological contamination and release. Accordingly, the loop will be mounted inside a safety enclosure. The safety enclosure will be an engineered structure capable of bearing the weight loads of the furnace, pump, and all other required equipment. The enclosure protects personnel from inadvertent contact with hot surfaces by providing physical isolation.

There are two options for the safety enclosure: ventilated and inert atmosphere. In the case of the ventilated enclosure, the enclosure will be continuously exhausted to provide negative pressure for drawing the room air through the enclosure. In the event of a leak or spill, this ensures potentially volatile hazardous materials do not escape into the room air. This also provides some convective cooling to the heated apparatus. Tritium containment strategies also frequently rely on continuous ventilation. The negative enclosure pressure helps ensure tritium permeating into the enclosure is swept through the exhaust. This option will require routine weekly beryllium smears on the external surfaces of the enclosure to ensure no beryllium species escape the enclosure.

In the case of an inert atmosphere glove box, no routine beryllium smears will be required on the external surfaces. However, an engineered cooling system will need to be designed and installed to prevent overheating of the internal components and structure.

Both options will require a combination of reactive oxidation catalyst bed, bubblers, getter beds, and HEPA filters for the exhaust stream to prevent the release of tritium and hazardous particulates.

## 4.4 Experiment Analysis

### 4.4.1 Test Section Scaling

The purpose of MSTTE is to test tritium transport in MSR-relevant conditions. Therefore, we have designed it attempting to match the range of dimensionless parameters  $Re$ ,  $W$ , and  $H$ , corresponding to the various salt-metal systems in the MSRE to appropriately size the test section. The experimental parameters assessed are the test section tube ID and wall thickness. The tube ID is sized with the  $Re$  number, and the wall thickness affects the permeation numbers  $H$  and  $W$ .

The first parameter to assess is the volumetric salt flow rate as a function of the test section tube ID to achieve MSRE relevant  $Re$  number. While the velocity decreases with an increase in ID to maintain a constant  $Re$  number, the salt flow rate increases proportionally with the ID due to the increase in surface area as shown in Figure 24.

The total loop pressure drop is calculated as a function of test section ID, and Figure 25 displays the results. Note, thermophysical properties of FLiBe are taken at 650°C for these calculations. In the limit of 0.5 in OD structural tubing for the loop (Figure 25A), the major losses through the structural tubing dominate the total head loss until the test section ID approaches 2 mm. In this configuration, the maximum achievable flow rate in the loop will be < 10 lpm. This considers the maximum head loss limit from the pumps used in the ORNL and UW-M loop designs. If the structural tubing is increased to 1 in. OD (Figure 24B), the maximum achievable flow rate increases to < 100 lpm, but this value has greater dependence on the test section ID. The Nagle C1-05-010 pump is designed to meet these specifications.

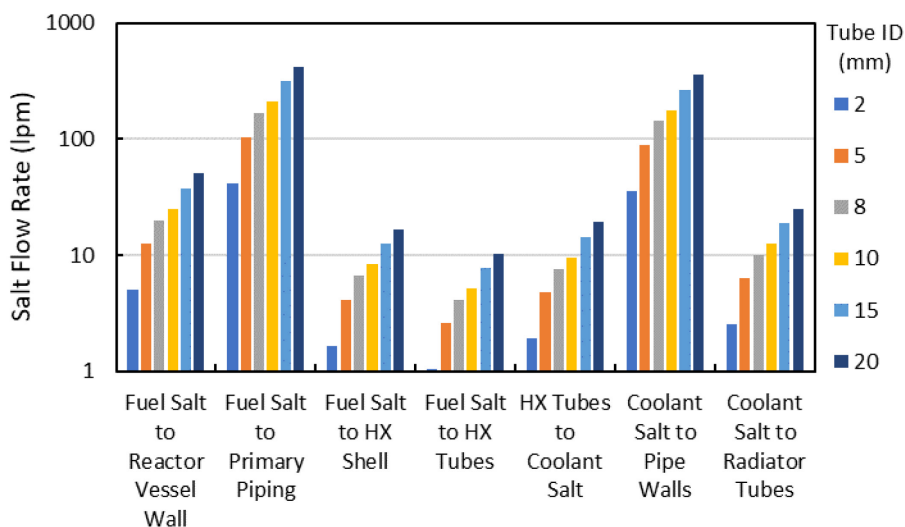


Figure 24. Calculation of FLiBe flow rate (lpm) as a function of test section ID (mm) to meet MSRE relevant  $Re$  number.

The next assessment identifies relevant tritium transport regimes for experimental parameters such as flow rate, test section ID, and test section wall thickness. The  $H$  number relates salt-phase mass transport resistance with surface reaction resistance on the structural metals. The mass transport coefficient is affected by flow rate, test section ID, and Henry's law constant for tritium solubility. The surface reactions are controlled by the chemistry and surface-species. Figure 26 reports  $H$  numbers as a function of salt flow rate and test section ID, specifically for Cases 1, 2, and 3 as described in Section 2.3. These cases were selected to span the upper and lower bound values of Henry's law constants for clean surfaces (Case 1 and 2) and for an oxidized surface with upper bound Henry's law constant (Case 3). For each



case, the mid-range of test section IDs (5–15 mm) achieves H numbers relevant to MSRE components. For a given test section ID, varying the salt flow rate will enable the span with relevant H numbers.

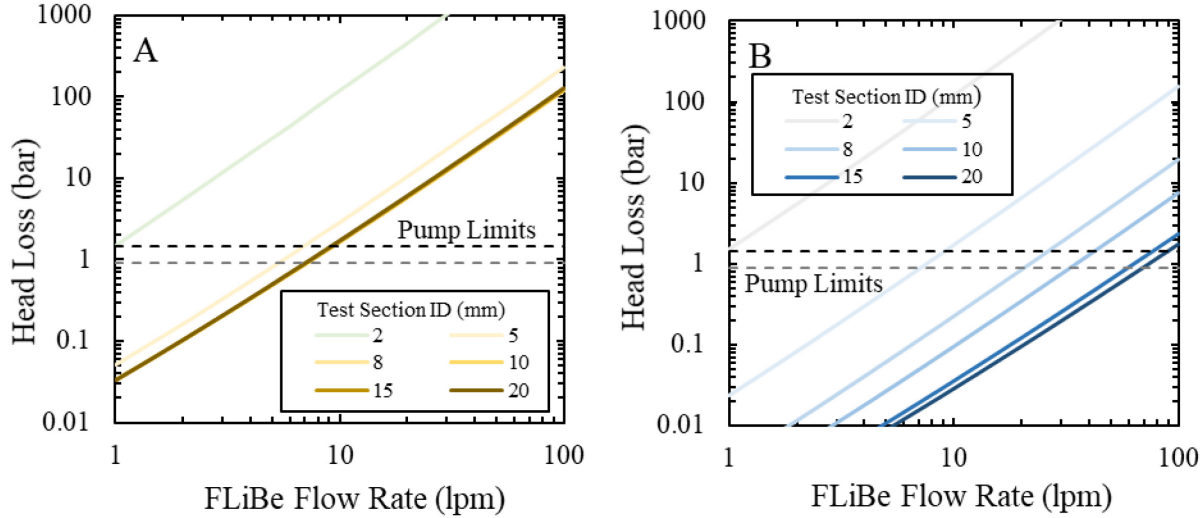


Figure 25. Total loop head loss calculations as a function of test section ID for (A) 0.5-inch OD loop structural tubing and (B) 1-inch OD loop structural tubing.

From the H number and Re number analysis, a test section ID of 8 mm is selected as the ideal parameter which will encompass relevant H numbers in achievable flow rates provided by a pump.

The permeation number (W) relates diffusive transport to surface reactions for hydrogen transport through metals. This is dependent on permeability, hydrogen partial pressure (concentration), wall thickness, and surface reaction (dissociation coefficient). Figure 27 presents the W number as a function of applied hydrogen pressure in the reverse permeator unit for varying wall thicknesses. The dissociation coefficients are taken for Cases 1, 3, and 5, which represent clean, heavily oxidized, and lightly oxidized surfaces, respectively. For these calculations, the applied hydrogen pressure in the reverse permeator is assumed to be in equilibrium with the hydrogen concentration in FLiBe.

The calculations show that MSRE relevant W numbers are achieved only in the limit of very low applied pressures ( $< 10$  Pa) and thin walls ( $< 0.5$  mm). This is due to the relatively low tritium concentration in FLiBe during MSRE operation. An assumption in this calculation is that the tritium concentration in the salt reaches equilibrium with the pressure applied in the reverse permeator unit. This assumption is accurate for a static system. However, for the looped nature of MSTTE, tritium concentration in the salt is a more complex function of the applied pressure in the reverse permeator unit, efficiency of the reverse permeator unit, extraction in the test section, off-gassing in the plenum, and permeation through the remainder of the structural material. This will result in a lower effective concentration and therefore more relevant W numbers will likely be obtained in the experiment. However, to best achieve relevant W number from the analysis conducted herein, we propose a test section made with 0.5 mm wall thickness.

Note this procedure was conducted using properties of Hastelloy N. This can be repeated for 316 SS or other candidate structural materials.

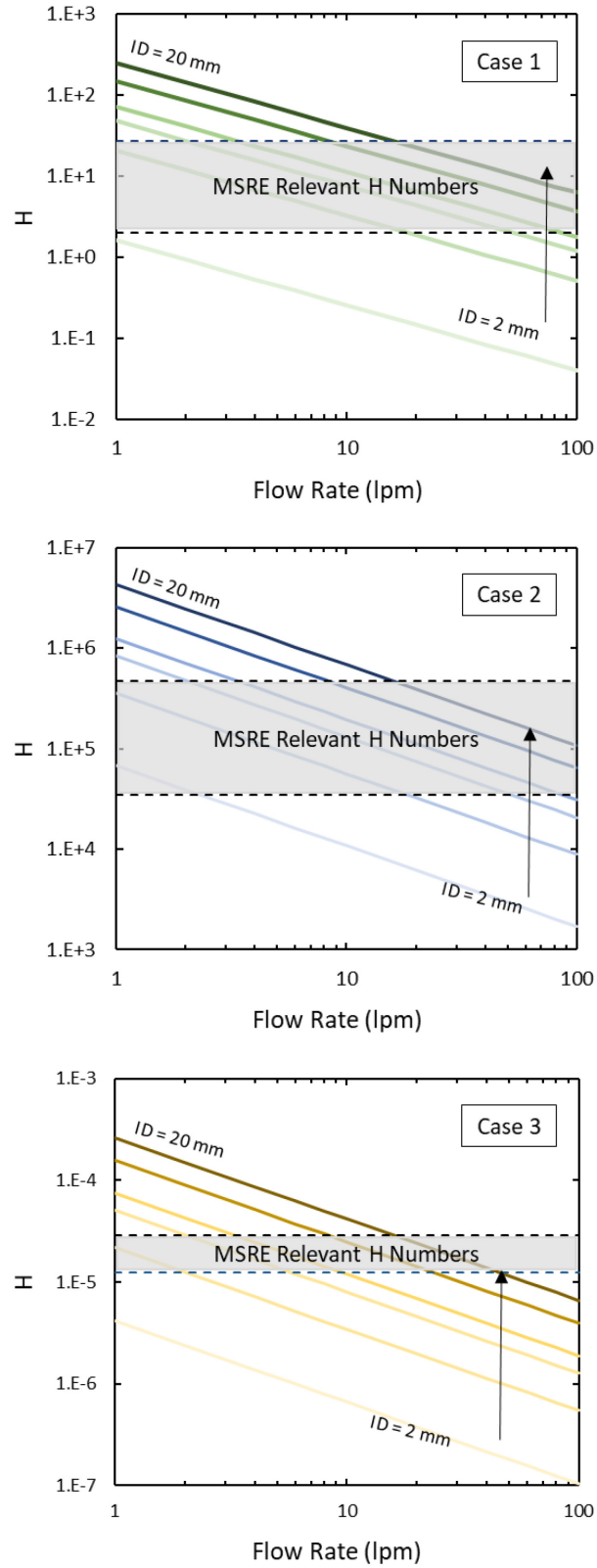


Figure 26. H number vs. FLiBe flow rate (lpm) for Cases 1–3. Calculated for IDs of 2, 5, 8, 10, 15, and 20 mm at a temperature of 650°C.

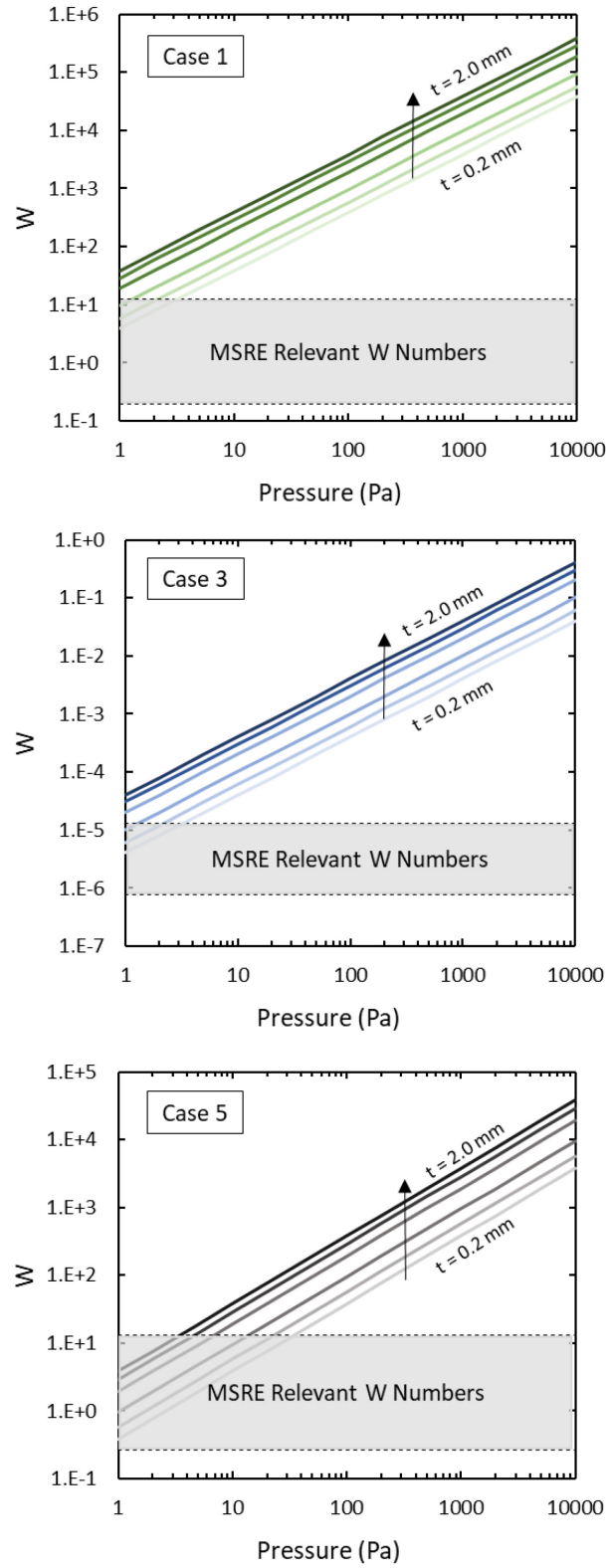


Figure 27. W number vs. hydrogen partial pressure (Pa) for Case 1, Case 3, and Case 5. Calculated for wall thicknesses of 0.2, 0.3, 0.5, 1, 1.5, and 2 mm at a temperature of 650°C.

## 5. Summary

Tritium is generated by neutron interactions with lithium and beryllium salts, such as FLiBe, and therefore in greater quantities in MSRs compared to other conventional reactor types. Tritium can readily transport through heated structural materials and escape into the secondary cooling systems, the surrounding rooms and buildings, and eventually into the environment. Therefore, understanding tritium transport and migration in the MSR system and developing predictive models is required to aid mitigation technology and the eventually the licensing of the reactors.

In this report, we have outlined a general theoretical description of tritium permeation loss mechanisms relevant to a MSR. Dimensionless numbers ( $W$ ,  $H$ , and  $W/H$ ) were used to assess the transport resistances for MSRE components. The analyzed transport phenomena included salt-phase mass transport, dissociation/recombination surface reactions on the metal surfaces, and diffusion through metals. The analysis showed surface reactions on the metal and salt-phase mass transport dominate the tritium transport processes in the MSRE components. The original MSRE report concluded that a  $1000\times$  reduction in permeability in the structural material was required to best predict the tritium distribution, which is consistent with the parameter studies done here.

To support analysis, a hydrogen and deuterium permeation campaign was performed on clean Hastelloy N from 500–700°C. The goal was to measure surface reaction rate constants; however, only diffusion-limited transport was observed at the lower pressure limits of the permeation apparatus. With the permeation results obtained, lower bounds on the values of the surface rate constants were also obtained and were comparable to surface rate constants reported for another high-Ni alloy. Measurements of permeability, diffusivity, and solubility of hydrogen and deuterium in Hastelloy N were obtained which adds a second data set to literature. The following are the results for deuterium:

$$\Phi_D = 2.40 \pm 0.70 \times 10^{-7} [\text{mol m}^{-1} \text{s}^{-1} \text{Pa}^{-0.5}] \exp\left(\frac{-62.2 \pm 1.8 [\text{kJ mol}^{-1}]}{RT}\right) \quad (28)$$

$$D_D = 1.96 \pm 0.25 \times 10^{-6} [\text{m}^2 \text{s}^{-1}] \exp\left(\frac{-54.8 \pm 0.8 [\text{kJ mol}^{-1}]}{RT}\right) \quad (29)$$

$$K_{S,D} = 0.12 \pm 0.03 [\text{mol m}^{-3} \text{Pa}^{-0.5}] \exp\left(\frac{-7.5 \pm 1.7 [\text{kJ mol}^{-1}]}{RT}\right) \quad (30)$$

Finally, the design of the MSTTE was presented. MSTTE would be a forced convection FLiBe loop with the purpose of testing tritium transport in the salt-metal system in relevant transport regimes. Major equipment and systems are presented including the test section, permeate gas analysis system, plenum, reverse permeator unit, molten-salt pump, flow meter and pressure gauge, supply tank, and differential gas sensor. Scaling analysis was performed with MSRE as a reference to assure the test section and pump size would be capable of attaining MSR-relevant Reynolds number and tritium permeation number ( $W$  and  $H$ ) regimes. The current design study was done on Hastelloy N; however, the analysis can be updated if 316 SS is determined to be a more relevant material for future MSR designs.

## 6. References

1. Humrickhouse, P. W. and T. F. Fuerst. 2020. "Tritium Transport Phenomena in Molten-Salt Reactors: Validation Data Needs and Research Plan." INL/EXT-20-59927, Idaho National Laboratory.
2. Ali-Khan, I., K. J. Dietz, F. G. Waelbroeck, and P. Wienhold. 1978. "The rate of hydrogen release out of clean metallic surfaces." *Journal of Nuclear Materials* 76–77, September–October: 337–343. [https://doi.org/10.1016/0022-3115\(78\)90167-8](https://doi.org/10.1016/0022-3115(78)90167-8).

3. Briggs, R. B. 1970. "Calculation of the Tritium Distribution in the MSRE." ORNL-CF-70-7-13, Oak Ridge National Laboratory.
4. Lee, H. 2010. "Compact Heat Exchangers." In *Thermal Design*, 240–381. Hoboken: John Wiley & Sons. Inc. <https://doi.org/10.1002/9780470949979.ch5>.
5. Romatoski, R. R. and L. W. Hu. 2017. "Fluoride salt coolant properties for nuclear reactor applications: A review." *Annals of Nuclear Energy* 109, November: 635–647. <https://doi.org/10.1016/j.anucene.2017.05.036>.
6. Calderoni, P., P. Sharpe, M. Hara, and Y. Oya. 2008. "Measurement of tritium permeation in flibe (2LiF–BeF<sub>2</sub>)." *Fusion Engineering and Design* 83, no. 7–9, December: 1331–1334. <https://doi.org/10.1016/j.fusengdes.2008.05.016>.
7. Briggs, R. B. 1971. "Additional Calculations of the Distribution of Tritium in the MSRE." ORNL-CF-71-7-8, Oak Ridge National Laboratory.
8. Haubenreich, P. N. 1970. "Tritium in the MSRE: Calculated Production Rates and Observed Amounts." ORNL-CF-70-2-7, Oak Ridge National Laboratory.
9. Dolan, K., S. Huang, M. Hackett, and L.-W. Hu. 2021. "Modeling Tritium Retention in Graphite for Fluoride-Salt-Cooled High-Temperature Reactors." *Nuclear Technology*, 1–21. <http://doi.org/10.1080/00295450.2020.1829428>.
10. Briggs, R. B. and R. B. Korsmeyer. 1970. "Distribution of Tritium in a 1000-Mw(e) MSBR." ORNL-CF-70-3-3, Oak Ridge National Laboratory, .
11. Stempien, J. D. 2015. "Tritium Transport, Corrosion, and Fuel Performance Modeling in the Fluoride Salt-Cooled High-Temperature Reactor (FHR)." Ph.D thesis, Massachusetts Institute of Technology. <http://hdl.handle.net/1721.1/103727>.
12. Stempien, J. D., R. G. Ballinger, and C. W. Forsberg. 2016. "An integrated model of tritium transport and corrosion in Fluoride Salt-Cooled High-Temperature Reactors (FHRs) – Part I: Theory and benchmarking." *Nuclear Engineering and Design* 310, December: 258–272. <https://doi.org/10.1016/j.nucengdes.2016.10.051>.
13. Altunoglu, A. K., D. A. Blackburn, N. S. J. Braithwaite, and D. M. Grant. 1991. "Permeation of hydrogen through nickel foils: surface reaction rates at low temperatures." *Journal of the Less Common Metals* 172–174, August: 718–726. [https://doi.org/10.1016/0022-5088\(91\)90195-A](https://doi.org/10.1016/0022-5088(91)90195-A).
14. Rota, E., F. Waelbroeck, P. Wienhold, and J. Winter. 1982. "Measurements of surface and bulk properties for the interaction of hydrogen with inconel 600." *Journal of Nuclear Materials* 111–112, November–December: 233–239. [https://doi.org/10.1016/0022-3115\(82\)90214-8](https://doi.org/10.1016/0022-3115(82)90214-8).
15. Perujo, A., K. Douglas, and E. Serra. 1996. "Low pressure tritium interaction with Inconel 625 and AISI 316 L stainless steel surfaces: an evaluation of the recombination and adsorption constants." *Fusion Engineering and Design* 31, no. 2 (June): 101–108. [https://doi.org/10.1016/0920-3796\(94\)00434-X](https://doi.org/10.1016/0920-3796(94)00434-X).
16. Esteban, G. A., A. Perujo, L. A. Sedano, F. Legarda, B. Mancinelli, and K. Douglas. 2002. "Diffusive transport parameters and surface rate constants of deuterium in Incoloy 800." *Journal of Nuclear Materials* 300, no. 1 (January): 1–6. [https://doi.org/10.1016/S0022-3115\(01\)00715-2](https://doi.org/10.1016/S0022-3115(01)00715-2).
17. Malinauskas, A. P. and D. M. Richardson. 1974. "The Solubilities of Hydrogen, Deuterium, and Helium in Molten Li<sub>2</sub>BeF<sub>4</sub>." *Industrial & Engineering Chemistry Fundamentals* 13, no. 3 (August): 242–245. <http://doi.org/10.1021/i160051a015>.
18. Louthan, M. R. and R. G. Derrick. 1975. "Hydrogen transport in austenitic stainless steel." *Corrosion Science* 15, no. 6, 565–577. [https://doi.org/10.1016/0010-938X\(75\)90022-0](https://doi.org/10.1016/0010-938X(75)90022-0).

19. Yamanishi, Y., T. Tanabe, and S. Imoto. 1983. "Hydrogen permeation and diffusion through pure Fe, pure Ni and Fe-Ni alloys." *Transactions of the Japan Institute of Metals* 24, no. 1, 49–58. <https://doi.org/10.2320/matertrans1960.24.49>.
  20. Zhang, D., W. Liu, and W. Liu. 2020. "Diffusion Characterization of Hydrogen Isotopes in Hastelloy N Alloy for the Application of Fluoride-Salt-Cooled High-Temperature Reactors (FHRs)." *Fusion Science and Technology* 76, no. 4 (May): 543–552. <http://doi.org/10.1080/15361055.2020.1725368>.
  21. Webb, R. W. 1965. "Permeation of hydrogen through metals." NAA-SR-10462, *Atomics International*.
  22. Strehlow, R. A. and H. C. Savage. 1974. "The Permeation of Hydrogen Isotopes through Structural Metals at Low Pressures and through Metals with Oxide Film Barriers." *Nuclear Technology* 22, no. 1, 127–137. <http://doi.org/10.13182/NT74-A16282>.
  23. Rader, J. D., D. K. Felde, J. McFarlane, M. S. Greenwood, A. L. Qualls, and P. Calderoni. 2017. "Tritium Management Loop Design Status." ORNL/TM-2017/511, Oak Ridge National Laboratory. <https://doi.org/10.2172/1427651>.
  24. Shimada, M. and R. J. Pawelko. 2018. "Tritium permeability measurement in hydrogen-tritium system." *Fusion Engineering and Design* 129, April: 134–139. <https://doi.org/10.1016/j.fusengdes.2018.02.033>.
  25. Shimada, M. and R. J. Pawelko. 2019. "Tritium permeability in polycrystalline tungsten." *Fusion Engineering and Design* 146, September: 1988–1992. <https://doi.org/10.1016/j.fusengdes.2019.03.083>.
  26. Yoder, G. L. et al. 2015. "High-Temperature Fluoride Salt Test Loop." ORNL/TM-2012/430, Oak Ridge National Laboratory. <https://doi.org/10.2172/1237612>.
  27. Sabharwall, P. et al. 2010. "Molten Salts for High Temperature Reactors: University of Wisconsin Molten Salt Corrosion and Flow Loop Experiments – Issues Identified and Path Forward." INL/EXT-10-18090, Idaho National Laboratory. <https://inldigitallibrary.inl.gov/sites/sti/sti/4502649.pdf>
  28. Utili, M., A. Aiello, L. Laffi, A. Malavasi, and I. Ricapito. 2016. "Investigation on efficiency of gas liquid contactor used as tritium extraction unit for HCLL-TBM Pb-16Li loop." *Fusion Engineering and Design* 109–111, November: 1–6. <https://doi.org/10.1016/j.fusengdes.2016.03.067>.
  29. Tosti, S., L. Farina, A. Pozio, A. Santucci, and D. Alique. 2021. "Study of a stainless steel porous membrane for recovering tritium from Pb-Li alloys: Assessment of mass transfer coefficient." *Fusion Engineering and Design* 168, July: 112423. <https://doi.org/10.1016/j.fusengdes.2021.112423>.
  30. IDECO. 2021. "IDECO Hydrogen-Analyser." Accessed June, 05 2021. <https://www.ideco-gmbh.de/index.php?d=844&page=005&lang=en&dev=0049>.
- 
- [1] P. W. Humrickhouse and T. F. Fuerst, "Tritium Transport Phenomena in Molten-Salt Reactors: Validation Data Needs and Research Plan," Idaho National Laboratory, INL/EXT-20-59927, 2020.
  - [2] I. Ali-Khan, K. J. Dietz, F. G. Waelbroeck, and P. Wienhold, "The rate of hydrogen release out of clean metallic surfaces," *Journal of Nuclear Materials*, vol. 76-77, pp. 337-343, 1978, doi: [https://doi.org/10.1016/0022-3115\(78\)90167-8](https://doi.org/10.1016/0022-3115(78)90167-8).
  - [3] R. B. Briggs, "Calculation of the Tritium Distribution in the MSRE," Oak Ridge National Laboratory, ORNL Central Files Number 70-7-13, 1970.

- [4] Lee, H. 2010. "Compact Heat Exchangers." in *Thermal Design*, 240-381. Hoboken: John Wiley & Sons. Inc. <https://doi.org/10.1002/9780470949979.ch5>.
- [5] R. R. Romatoski and L. W. Hu, "Fluoride salt coolant properties for nuclear reactor applications: A review," *Annals of Nuclear Energy*, vol. 109, pp. 635-647, 2017, doi: <https://doi.org/10.1016/j.anucene.2017.05.036>.
- [6] P. Calderoni, P. Sharpe, M. Hara, and Y. Oya, "Measurement of tritium permeation in flibe (2LiF–BeF<sub>2</sub>)," *Fusion Engineering and Design*, vol. 83, no. 7, pp. 1331-1334, 2008, doi: <https://doi.org/10.1016/j.fusengdes.2008.05.016>.
- [7] R. B. Briggs, "Additional Calculations of the Distribution of Tritium in the MSRE," Oak Ridge National Laboratory, ORNL Central Files Number 71-7-8, 1971.
- [8] P. N. Haubenreich, "Tritium in the MSRE: Calculated Production Rates and Observed Amounts," Oak Ridge National Laboratory, ORNL Central Files Number 70-2-7, 1970.
- [9] K. Dolan, S. Huang, M. Hackett, and L.-W. Hu, "Modeling Tritium Retention in Graphite for Fluoride-Salt-Cooled High-Temperature Reactors," *Nuclear Technology*, pp. 1-21, 2021, doi: 10.1080/00295450.2020.1829428.
- [10] R. B. Briggs and R. B. Korsmeyer, "Distribution of Tritium in a 1000-Mw(e) MSBR," Oak Ridge National Laboratory, ORNL Central Files Number 70-3-3, 1970.
- [11] J. D. Stempien, "Tritium Transport, Corrosion, and Fuel Performance Modeling in the Fluoride Salt-Cooled High-Temperature Reactor (FHR)," Doctor of Philosophy, Massachusetts Institute of Technology, 2015.
- [12] J. D. Stempien, R. G. Ballinger, and C. W. Forsberg, "An integrated model of tritium transport and corrosion in Fluoride Salt-Cooled High-Temperature Reactors (FHRs) – Part I: Theory and benchmarking," *Nuclear Engineering and Design*, vol. 310, pp. 258-272, 2016, doi: <https://doi.org/10.1016/j.nucengdes.2016.10.051>.
- [13] A. K. Altunoglu, D. A. Blackburn, N. S. J. Braithwaite, and D. M. Grant, "Permeation of hydrogen through nickel foils: surface reaction rates at low temperatures," *Journal of the Less Common Metals*, vol. 172-174, pp. 718-726, 1991, doi: [https://doi.org/10.1016/0022-5088\(91\)90195-A](https://doi.org/10.1016/0022-5088(91)90195-A).
- [14] E. Rota, F. Waelbroeck, P. Wienhold, and J. Winter, "Measurements of surface and bulk properties for the interaction of hydrogen with inconel 600," *Journal of Nuclear Materials*, vol. 111-112, pp. 233-239, 1982, doi: [https://doi.org/10.1016/0022-3115\(82\)90214-8](https://doi.org/10.1016/0022-3115(82)90214-8).
- [15] A. Perujo, K. Douglas, and E. Serra, "Low pressure tritium interaction with Inconel 625 and AISI 316 L stainless steel surfaces: an evaluation of the recombination and adsorption constants," *Fusion Engineering and Design*, vol. 31, no. 2, pp. 101-108, 1996, doi: [https://doi.org/10.1016/0920-3796\(94\)00434-X](https://doi.org/10.1016/0920-3796(94)00434-X).
- [16] G. A. Esteban, A. Perujo, L. A. Sedano, F. Legarda, B. Mancinelli, and K. Douglas, "Diffusive transport parameters and surface rate constants of deuterium in Incoloy 800," *Journal of Nuclear Materials*, vol. 300, no. 1, pp. 1-6, 2002, doi: [https://doi.org/10.1016/S0022-3115\(01\)00715-2](https://doi.org/10.1016/S0022-3115(01)00715-2).
- [17] A. P. Malinauskas and D. M. Richardson, "The Solubilities of Hydrogen, Deuterium, and Helium in Molten Li<sub>2</sub>BeF<sub>4</sub>," *Industrial & Engineering Chemistry Fundamentals*, vol. 13, no. 3, pp. 242-245, 1974, doi: 10.1021/i160051a015.
- [18] M. R. Louthan and R. G. Derrick, "Hydrogen transport in austenitic stainless steel," *Corrosion Science*, vol. 15, no. 6, pp. 565-577, 1975, doi: [https://doi.org/10.1016/0010-938X\(75\)90022-0](https://doi.org/10.1016/0010-938X(75)90022-0).
- [19] Y. Yamanishi, T. Tanabe, and S. Imoto, "Hydrogen permeation and diffusion through pure Fe, pure Ni and Fe-Ni alloys," *Transactions of the Japan Institute of Metals*, vol. 24, no. 1, pp. 49-58, 1983.
- [20] D. Zhang, W. Liu, and W. Liu, "Diffusion Characterization of Hydrogen Isotopes in Hastelloy N Alloy for the Application of Fluoride-Salt-Cooled High-Temperature Reactors (FHRs)," *Fusion Science and Technology*, vol. 76, no. 4, pp. 543-552, 2020, doi: 10.1080/15361055.2020.1725368.

- [21] R. W. Webb, "Permeation of hydrogen through metals," Atomics International, NAA-SR-10462, 1965.
- [22] R. A. Strehlow and H. C. Savage, "The Permeation of Hydrogen Isotopes through Structural Metals at Low Pressures and through Metals with Oxide Film Barriers," *Nuclear Technology*, vol. 22, no. 1, pp. 127-137, 1974, doi: 10.13182/NT74-A16282.
- [23] J. D. Rader, D. K. Felde, J. McFarlane, M. S. Greenwood, A. L. Qualls, and P. Calderoni, "Tritium Management Loop Design Status," Oak Ridge National Laboratory, ORNL/TM-2017/511, 2017.
- [24] M. Shimada and R. J. Pawelko, "Tritium permeability measurement in hydrogen-tritium system," *Fusion Engineering and Design*, vol. 129, pp. 134-139, 2018, doi: <https://doi.org/10.1016/j.fusengdes.2018.02.033>.
- [25] M. Shimada and R. J. Pawelko, "Tritium permeability in polycrystalline tungsten," *Fusion Engineering and Design*, vol. 146, pp. 1988-1992, 2019, doi: <https://doi.org/10.1016/j.fusengdes.2019.03.083>.
- [26] G. L. Yoder *et al.*, "High-Temperature Fluoride Salt Test Loop," Oak Ridge National Laboratory, ORNL/TM-2012/430, 2015.
- [27] P. Sabharwall *et al.*, "Molten Salts for High Temperature Reactors: University of Wisconsin Molten Salt Corrosion and Flow Loop Experiments – Issues Identified and Path Forward," Idaho National Laboratory, INL/EXT-10-18090, 2010. [Online]. Available: <https://inldigitallibrary.inl.gov/sites/sti/sti/4502649.pdf>
- [28] M. Utili, A. Aiello, L. Laffi, A. Malavasi, and I. Ricapito, "Investigation on efficiency of gas liquid contactor used as tritium extraction unit for HCLL-TBM Pb-16Li loop," *Fusion Engineering and Design*, vol. 109-111, pp. 1-6, 2016, doi: <https://doi.org/10.1016/j.fusengdes.2016.03.067>.
- [29] S. Tosti, L. Farina, A. Pozio, A. Santucci, and D. Alique, "Study of a stainless steel porous membrane for recovering tritium from Pb-Li alloys: Assessment of mass transfer coefficient," *Fusion Engineering and Design*, vol. 168, p. 112423, 2021, doi: <https://doi.org/10.1016/j.fusengdes.2021.112423>.
- [30] "IDECO Hydrogen-Analyser." <https://www.ideco-gmbh.de/index.php?d=844&page=005&lang=en&dev=0049> (accessed 06/05/2021).